J. Fluid Mech. (2014), *vol.* 746, *pp.* 53–84. © Cambridge University Press 2014
doi:10.1017/jfm.2014.79

Solving the Boltzmann equation deterministically by the fast spectral method: application to gas microflows

Lei Wu[1], **Jason M. Reese**[2] **and Yonghao Zhang**[1,†]

[1]James Weir Fluids Laboratory, Department of Mechanical and Aerospace Engineering, University of Strathclyde, Glasgow G1 1XJ, UK

[2]School of Engineering, University of Edinburgh, Edinburgh EH9 3JL, UK

(Received 15 August 2013; revised 28 January 2014; accepted 5 February 2014; first published online 28 March 2014)

Based on the fast spectral approximation to the Boltzmann collision operator, we present an accurate and efficient deterministic numerical method for solving the Boltzmann equation. First, the linearized Boltzmann equation is solved for Poiseuille and thermal creep flows, where the influence of different molecular models on the mass and heat flow rates is assessed, and the Onsager–Casimir relation at the microscopic level for large Knudsen numbers is demonstrated. Recent experimental measurements of mass flow rates along a rectangular tube with large aspect ratio are compared with numerical results for the linearized Boltzmann equation. Then, a number of two-dimensional microflows in the transition and free-molecular flow regimes are simulated using the nonlinear Boltzmann equation. The influence of the molecular model is discussed, as well as the applicability of the linearized Boltzmann equation. For thermally driven flows in the free-molecular regime, it is found that the magnitudes of the flow velocity are inversely proportional to the Knudsen number. The streamline patterns of thermal creep flow inside a closed rectangular channel are analysed in detail: when the Knudsen number is smaller than a critical value, the flow pattern can be predicted based on a linear superposition of the velocity profiles of linearized Poiseuille and thermal creep flows between parallel plates. For large Knudsen numbers, the flow pattern can be determined using the linearized Poiseuille and thermal creep velocity profiles at the critical Knudsen number. The critical Knudsen number is found to be related to the aspect ratio of the rectangular channel.

Key words: computational methods, micro-/nano-fluid dynamics, rarefied gas flow

1. Introduction

The Knudsen number Kn, the ratio of the molecular mean free path λ to the characteristic flow length ℓ, is an important parameter in rarefied gas dynamics. The Navier–Stokes–Fourier (NSF) equations based on the continuum fluid hypothesis can usually be used up to $Kn \sim 0.001$. (There are some exceptions where the NSF equations do not describe the gas dynamics properly even when $Kn \to 0$, for example the ghost effect induced by a spatially periodic variation of the wall temperature,

† Email address for correspondence: yonghao.zhang@strath.ac.uk

https://doi.org/10.1017/jfm.2014.79 Published online by Cambridge University Press

see Sone (2002).) When Kn is larger, the continuum hypothesis breaks down and the NSF equations fail to capture the non-conventional behaviour of the rarefied flow. This situation is most frequently encountered in high-altitude aerodynamics and in the vacuum industry (where λ is large), and in micro/nano-electromechanical systems (where ℓ is small). The Boltzmann equation (BE) is a fundamental model at the microscopic level describing rarefied gas dynamics for the full range of Knudsen number (Cercignani 1990). It uses the velocity distribution function (VDF) defined in a six-dimensional phase space to describe the system state, along with the Boltzmann collision operator (BCO) to model the intermolecular interactions. The BE is complicated, which makes it highly desirable to use macroscopic equations like the NSF model. In the past, Burnett models and Grad moment equations have been derived from the BE. While the Burnett models are intrinsically unstable (Garcia-Colin, Velasco & Uribe 2008), regularized Grad moment equations have been applied up to the transition flow regime for some specific problems (Gu & Emerson 2009; Rana, Torrilhon & Struchtrup 2013).

For moderately or highly rarefied gases, it is necessary to solve the BE numerically. The direct simulation Monte Carlo (DSMC) method (Bird 1994) is the prevailing technique. It is efficient for high-speed flows, but becomes computationally time-consuming in microflow simulations where the flow velocity is far smaller than the thermal velocity. To tackle this difficulty, information-preservation (Fan & Shen 2001; Masters & Ye 2007) and low-noise (Baker & Hadjiconstantinou 2005; Homolle & Hadjiconstantinou 2007; Radtke, Hadjiconstantinou & Wagner 2011) DSMC methods have been proposed. The information-preserving method introduces information quantities (such as the information velocity and information temperature) to reduce the statistical noise, which has proven highly effective. However, its convergence to the BE has not been rigorously shown. The low-noise DSMC method significantly improves the computational efficiency of the original DSMC method by simulating only the deviation from the equilibrium state. To our knowledge, for microflow simulations, it is currently the most efficient stochastic method to solve the BE (Radtke *et al.* 2011).

The deterministic numerical solution of the BE is, however, theoretically the best method to resolve small signals, because it is not subject to fluctuations. However, the high computational cost in the approximation of the BCO restricts the number of discrete velocity grids one can use; this does not cause problems when the VDF is smooth, but it does lead to failure at large Kn where discontinuities and/or fine structures exist. Therefore, a deterministic numerical method allowing a large number of discrete velocity grids but with reduced computational cost is needed for highly rarefied gas flow simulations.

The fast spectral method (FSM), proposed by Mouhot & Pareschi (2006), and improved by Wu *et al.* (2013), is one such method. The FSM handles the binary molecular collisions in frequency space instead of velocity space, where the Fourier spectrum of the BCO appears as a convolved sum of the weighted spectrum of the VDF. When this sum is carried out directly, the computational cost is $O(N_\xi^6)$, where N_ξ is the number of frequency components in one direction. The main idea of the FSM is to separate the frequency components in the weighted function, so that the convolution theorem can be applied, reducing the computational cost to $O(M^2 N_\xi^3 \log N_\xi)$, where the number of discrete angles M is far less than N_ξ. This separation requires special forms of the collision kernel. In our previous paper (Wu *et al.* 2013), these special forms were constructed and validated, making the FSM applicable to all inverse power-law (IPL) potentials (except for the Coulomb potential) and the Lennard-Jones (LJ) potential.

https://doi.org/10.1017/jfm.2014.79 Published online by Cambridge University Press

In this present paper we explore the features of the FSM for microflow simulation. We assess the influence of the discrete velocity grids, the number of frequency components, and the number of discrete angles M on the accuracy of the FSM. Based on this accurate and efficient numerical method, a number of two-dimensional microflows are simulated, and the influence of the molecular models is discussed. The asymptotic behaviour of thermally driven flows in the free-molecular regime is investigated and, specifically, the flow pattern of the thermal creep flow inside a closed rectangular channel is studied in detail. A new criterion and method are proposed to predict the flow pattern in closed rectangular channels of arbitrary aspect ratio and Knudsen number.

The paper is organized as follows: the BE with special anisotropic collision kernels is introduced in § 2, and the approximation of the (nonlinear and linear) BCOs by the FSM is presented in § 3. In § 4, based on the linearized BE, the numerical accuracy of the FSM is evaluated and its computational efficiency is demonstrated for both Poiseuille and thermal creep flows. The influence of different molecular models on the flow rates is discussed and the accuracy of the special collision kernel for the LJ potential is evaluated. In § 5, based on the nonlinear BE, a number of two-dimensional flows are simulated and the influence of the molecular model is assessed. A new scaling law for the flow velocity is proposed for thermally driven flows in the free-molecular regime. The flow field of the thermal creep flow inside a closed rectangular channel is also investigated. Finally, we conclude this paper in § 6.

2. The Boltzmann equation

2.1. *The nonlinear Boltzmann equation*

In this paper we consider a monatomic gas. In reality, the intermolecular interaction is best described by the (6–12) LJ potential. For simplicity, however, IPL molecular models have been introduced, and are widely used by researchers. Hence we first consider IPL intermolecular potentials. According to the Chapman–Enskog expansion (Chapman & Cowling 1970), the shear viscosity μ is proportional to T^{ω}, with T being the temperature and ω the viscosity index. Special collision kernels can be used to recover not only the value of the shear viscosity but also its temperature dependence (Wu *et al.* 2013). We therefore consider the BE

$$\frac{\partial f}{\partial t} + \boldsymbol{v} \cdot \frac{\partial f}{\partial \boldsymbol{x}} = Q(f, f_*), \tag{2.1}$$

where the BCO is given by

$$Q(f, f_*) \equiv \iint B(|\boldsymbol{u}|, \theta)(f'_* f' - f_* f)\mathrm{d}\Omega \mathrm{d}\boldsymbol{v}_*, \tag{2.2}$$

with the following form of the collision kernel:

$$B(|\boldsymbol{u}|, \theta) = \frac{|\boldsymbol{u}|^{\alpha}}{K} \sin^{\alpha+\gamma-1}\left(\frac{\theta}{2}\right) \cos^{-\gamma}\left(\frac{\theta}{2}\right), \tag{2.3}$$

where $\alpha = 2(1-\omega)$, θ is the deflection angle, and γ is a free parameter.

The BE above is given in dimensionless form: the spatial variable $\boldsymbol{x}$ is normalized by a characteristic flow length ℓ; the molecular velocity $\boldsymbol{v}$ and relative velocity $\boldsymbol{u}$ are normalized by the most probable molecular speed $v_m = \sqrt{2k_B T_0/m}$, with k_B the Boltzmann constant, T_0 the reference temperature, and m the molecular mass. The

https://doi.org/10.1017/jfm.2014.79 Published online by Cambridge University Press

time t is normalized by ℓ/v_m, while the VDF is normalized by n_0/v_m^3, where n_0 is the reference molecular number density. The subscript $*$ represents the second molecule in the binary collision, the superscript prime stands for quantities after the collision, and Ω is the solid angle. Finally, to recover the shear viscosity, we have

$$K = \frac{2^{7-\omega}}{5}\Gamma\left(\frac{\alpha+\gamma+3}{2}\right)\Gamma\left(2-\frac{\gamma}{2}\right)Kn, \tag{2.4}$$

where

$$Kn = \frac{\mu(T_0)}{n_0\ell}\sqrt{\frac{\pi}{2mk_BT_0}}, \tag{2.5}$$

is the unconfined Knudsen number and Γ is the gamma function. Note that the rarefaction parameter Kn is $15\pi/2(7-2\omega)(5-2\omega)$ times larger than the Knudsen number Kn_{vhs}, where λ is defined by equation (4.52) in the book by Bird (1994). Also note that sometimes the parameter δ is used (Sharipov & Seleznev 1994, 1998), which is related to the unconfined Knudsen number Kn by

$$\delta = \frac{\sqrt{\pi}}{2Kn}. \tag{2.6}$$

For realistic (6–12) LJ potentials, the shear viscosity from the Chapman–Enskog expansion is not a power-law function of temperature; only in a small temperature range could the viscosity be described by a single power-law function of temperature. For instance, for helium and argon, in the temperature range $293 < T < 373$ K, it has been suggested to use $\omega = 0.66$ and $\omega = 0.81$, respectively (Chapman & Cowling 1970; Bird 1994). Over a broader temperature range, the single IPL model may not work well. Note that if we use the realistic collision kernel given by Sharipov & Bertoldo (2009*a*), the calculation of the weighted function becomes very complicated and, moreover, the efficiency of the FSM is reduced by one order of magnitude. Therefore, we propose using the following collision kernel:

$$B(|\boldsymbol{u}|,\theta) = \frac{5\sum_{j=1}^{3} b_j(k_BT_0/2\epsilon)^{(\alpha_j-1)/2}\sin^{\alpha_j-1}(\theta/2)|\boldsymbol{u}|^{\alpha_j}/\Gamma\left(\frac{\alpha_j+3}{2}\right)}{64\sqrt{2}Kn\sum_{j=1}^{3} b_j(k_BT_0/\epsilon)^{(\alpha_j-1)/2}}, \tag{2.7}$$

to approximate that of the realistic (6–12) LJ potential (Wu *et al.* 2013), where $b_1 = 407.4$, $b_2 = -811.9$, $b_3 = 414.4$, $\alpha_1 = 0.2$, $\alpha_2 = 0.1$, $\alpha_3 = 0$, and ϵ is the potential depth. This expression can recover the shear viscosity for the LJ potential over the temperature range $1 < k_BT/\epsilon < 25$, and produce accurate macroscopic quantities and microscopic VDFs in normal shock waves when compared to both experimental data and molecular dynamics simulations (Wu *et al.* 2013). Hereafter, the BE using the approximated collision kernel (2.7) will be called the LJ model, and the accuracy of this model in microflow simulations will be assessed.

2.2. *The linearized Boltzmann equation*

If the state of the gas is weakly non-equilibrium, the nonlinear BE (2.1) can be linearized. We express the VDF then as

$$f(t,\boldsymbol{x},\boldsymbol{v}) = f_{eq} + h(t,\boldsymbol{x},\boldsymbol{v}), \tag{2.8}$$

https://doi.org/10.1017/jfm.2014.79 Published online by Cambridge University Press

where

$$f_{eq}(\boldsymbol{v}) = \frac{\exp(-|\boldsymbol{v}|^2)}{\pi^{3/2}} \tag{2.9}$$

is the global equilibrium velocity distribution function, and $h(t, \boldsymbol{x}, \boldsymbol{v})$ represents the deviation from global equilibrium satisfying $|h| \ll 1$. The nonlinear BE is then linearized to

$$\frac{\partial h}{\partial t} + \boldsymbol{v} \cdot \frac{\partial h}{\partial \boldsymbol{x}} = \mathscr{L}_g(h) - \nu_{eq}(v)h, \tag{2.10}$$

where

$$\mathscr{L}_g(h) = \iint B(|\boldsymbol{u}|, \theta)[f_{eq}(\boldsymbol{v}')h(\boldsymbol{v}'_*) + f_{eq}(\boldsymbol{v}'_*)h(\boldsymbol{v}') - f_{eq}(\boldsymbol{v})h(\boldsymbol{v}_*)]\mathrm{d}\Omega\,\mathrm{d}\boldsymbol{v}_*, \tag{2.11}$$

which can be viewed as a linear gain term, and

$$\nu_{eq}(v) = \iint B(|\boldsymbol{u}|, \theta) f_{eq}(\boldsymbol{v}_*)\mathrm{d}\Omega\,\mathrm{d}\boldsymbol{v}_* \tag{2.12}$$

is the equilibrium collision frequency.

3. The fast spectral method

The five-fold integral BCO poses a challenge for the numerical solution of the BE. Unlike the discrete velocity method, which handles the binary collision in velocity space, the FSM works in a corresponding frequency space, where the VDF and BCO are expanded in Fourier series. The discrete velocity grid points can be non-uniform to capture discontinuities; however, in order to take advantage of fast Fourier transform (FFT)-based convolution, the frequency components should be uniformly distributed, i.e.

$$\left.\begin{aligned} f(\boldsymbol{v}) &= \sum_{\boldsymbol{j}=-\boldsymbol{N}/2}^{\boldsymbol{N}/2-1} \hat{f}_{\boldsymbol{j}} \exp(\mathrm{i}\xi_{\boldsymbol{j}} \cdot \boldsymbol{v}), \\ \hat{f}_{\boldsymbol{j}} &= \frac{1}{V_{\mathscr{D}}} \int_{\mathscr{D}} f(\boldsymbol{v}) \exp(-\mathrm{i}\xi_{\boldsymbol{j}} \cdot \boldsymbol{v})\mathrm{d}\boldsymbol{v}, \end{aligned}\right\} \tag{3.1}$$

where i is the imaginary unit, $\boldsymbol{N} = (N'_1, N'_2, N'_3)$, the equidistant frequency components are $\xi_{\boldsymbol{j}} = \boldsymbol{j}\pi/L$ with $\boldsymbol{j} = (j_1, j_2, j_3)$ and L being the maximum truncated velocity, and $\mathscr{D}$ is the truncated velocity domain with $V_{\mathscr{D}}$ its volume. The velocity domain is discretized by $N_1 \times N_2 \times N_3$ points and the spectrum $\hat{f}$ of the VDF can be calculated numerically by the trapezoidal rule. Note that the number of velocity grid points is usually larger than the number of frequency components.

The BCO and its Fourier spectrum $\hat{Q}$ are also expanded by Fourier series. The $\boldsymbol{j}$th Fourier mode of the BCO is related to the spectrum $\hat{f}$ as follows (Wu *et al.* 2013):

$$\hat{Q}(\boldsymbol{j}) = \frac{1}{V_{\mathscr{D}}} \int_{\mathscr{D}} Q(f, f_*) \exp(-\mathrm{i}\xi_{\boldsymbol{j}} \cdot \boldsymbol{v})\mathrm{d}\boldsymbol{v} = \sum_{\substack{\boldsymbol{l}+\boldsymbol{m}=\boldsymbol{j} \\ \boldsymbol{l},\boldsymbol{m}=-\boldsymbol{N}/2}}^{\boldsymbol{N}/2-1} \hat{f}_{\boldsymbol{l}}\hat{f}_{\boldsymbol{m}}[\beta(\boldsymbol{l}, \boldsymbol{m}) - \beta(\boldsymbol{m}, \boldsymbol{m})], \tag{3.2}$$

where $\boldsymbol{l} = (l_1, l_2, l_3)$, $\boldsymbol{m} = (m_1, m_2, m_3)$, and $\beta(\boldsymbol{l}, \boldsymbol{m})$ is the weighted function. For the collision kernel (2.3) for IPL potentials, the frequency components $\xi_{\boldsymbol{l}}$ and $\xi_{\boldsymbol{m}}$ in the

https://doi.org/10.1017/jfm.2014.79 Published online by Cambridge University Press

weighted function can be separated as

$$\beta(\boldsymbol{l},\boldsymbol{m})_{IPL} \simeq \frac{4}{K}\sum_{p,q=1}^{M}\psi_\gamma\left\{\sqrt{|\xi_{\boldsymbol{m}}|^2-(\xi_{\boldsymbol{m}}\cdot\boldsymbol{e}_{\theta_p,\varphi_q})^2}\right\}\omega_p\omega_q\sin\theta_p\phi_{\alpha+\gamma}(\xi_{\boldsymbol{l}}\cdot\boldsymbol{e}_{\theta_p,\varphi_q}), \tag{3.3}$$

while for the collision kernel (2.7) to approximate the LJ potential, we have

$$\begin{aligned}\beta(\boldsymbol{l},\boldsymbol{m})_{LJ} \simeq\ & \frac{5}{16\sqrt{2}Kn\sum_{j=1}^{3}b_j(k_BT_0/\epsilon)^{(\alpha_j-1)/2}}\sum_{p,q=1}^{M}\psi_\gamma\left\{\sqrt{|\xi_{\boldsymbol{m}}|^2-(\xi_{\boldsymbol{m}}\cdot\boldsymbol{e}_{\theta_p,\varphi_q})^2}\right\}\\ &\times\omega_p\omega_q\sin\theta_p\sum_{j=1}^{3}b_j(k_BT_0/2\epsilon)^{(\alpha_j-1)/2}\phi_{\alpha_j}(\xi_{\boldsymbol{l}}\cdot\boldsymbol{e}_{\theta_p,\varphi_q})/\Gamma\left(\frac{\alpha_j+3}{2}\right),\end{aligned} \tag{3.4}$$

where θ_p (φ_q) and ω_p (ω_q) are the p (q)th point and weight in the Gauss–Legendre quadrature, respectively, with $\theta,\varphi\in[0,\pi]$; $\boldsymbol{e}_{\theta_p,\varphi_q}=(\sin\theta_p\cos\varphi_q,\sin\theta_p\sin\varphi_q,\cos\theta_p)$, $\phi_{\alpha+\gamma}(s)=2\int_0^R\rho^{\alpha+\gamma}\cos(\rho s)\,\mathrm{d}\rho$, and $\psi_\gamma(s)=2\pi\int_0^R\rho^{1-\gamma}J_0(\rho s)\mathrm{d}\rho$. Here $R=2\sqrt{2}L/(2+\sqrt{2})$ is chosen approximately as the average of its minimum allowed value $2\sqrt{2}L/(3+\sqrt{2})$ and its maximum allowed value L (see figure 5 in Wu *et al.* 2013), and J_0 is the zeroth-order Bessel function.

For conventional spectral methods (Pareschi & Russo 2000; Gamba & Tharkabhushanam 2009), (3.2) is calculated by direct summation, with a computational cost $O(N_1'^2N_2'^2N_3'^2)$. However, if the FFT-based convolution is applied, the computational cost is reduced to $O(M^2N_1'N_2'N_3'\log(N_1'N_2'N_3'))$. The number of discrete angles M controls the computational cost and the numerical accuracy. It will be shown below that $M=6$ produces sufficiently accurate results. Hence the FSM is significantly faster than conventional spectral methods. Note that the computational cost of the IPL and LJ models is exactly the same.

When the spectrum of the BCO is obtained, we calculate the BCO through the following equation:

$$Q(f,f_*)=\sum_{\boldsymbol{j}=-\boldsymbol{N}/2}^{\boldsymbol{N}/2-1}\hat{Q}(\boldsymbol{j})\exp(\mathrm{i}\xi_{\boldsymbol{j}}\cdot\boldsymbol{v}). \tag{3.5}$$

Now we consider the fast spectral approximation of the linearized collision operator. The equilibrium collision frequency can be calculated analytically. For the linearized gain term $\mathscr{L}_g$, when the IPL potential is considered, the $\boldsymbol{j}$th Fourier mode of $\mathscr{L}_g$ is

$$\begin{aligned}\hat{\mathscr{L}}_g(\boldsymbol{j}) \approx\ & \frac{4}{K}\sum_{p,q=1}^{M}\sum_{\substack{\boldsymbol{l}+\boldsymbol{m}=\boldsymbol{j}\\ \boldsymbol{l},\boldsymbol{m}=-\boldsymbol{N}/2}}^{\boldsymbol{N}/2-1}\omega_p\omega_q\hat{f}_{eq}(\boldsymbol{l})\phi_{\alpha+\gamma}(\xi_{\boldsymbol{l}},\theta_p,\varphi_q)\hat{h}_{\boldsymbol{m}}\psi_\gamma(\xi_{\boldsymbol{m}},\theta_p,\varphi_q)\sin\theta_p\\ &+\frac{4}{K}\sum_{p,q=1}^{M}\sum_{\substack{\boldsymbol{l}+\boldsymbol{m}=\boldsymbol{j}\\ \boldsymbol{l},\boldsymbol{m}=-\boldsymbol{N}/2}}^{\boldsymbol{N}/2-1}\omega_p\omega_q\hat{h}_{\boldsymbol{l}}\phi_{\alpha+\gamma}(\xi_{\boldsymbol{l}},\theta_p,\varphi_q)\hat{f}_{eq}(\boldsymbol{m})\psi_\gamma(\xi_{\boldsymbol{m}},\theta_p,\varphi_q)\sin\theta_p\\ &-\frac{4}{K}\sum_{\substack{\boldsymbol{l}+\boldsymbol{m}=\boldsymbol{j}\\ \boldsymbol{l},\boldsymbol{m}=-\boldsymbol{N}/2}}^{\boldsymbol{N}/2-1}\hat{f}_{eq}(\boldsymbol{l})\hat{h}_{\boldsymbol{m}}\phi_{loss},\end{aligned} \tag{3.6}$$

https://doi.org/10.1017/jfm.2014.79 Published online by Cambridge University Press

where $\phi_{loss} = \sum_{p,q=1}^{M} \omega_p \omega_q \phi_{\alpha+\gamma}(\xi_{\boldsymbol{m}}, \theta_p, \varphi_q)\psi_\gamma(\xi_{\boldsymbol{m}}, \theta_p, \varphi_q) \sin\theta_p$ and $\hat{h}$ is the spectrum of the VDF h. For the LJ collision kernel (2.7), the $\boldsymbol{j}$th Fourier mode of the linear gain term can be obtained in a similar way.

Note that each term on the right-hand side of (3.6) is a convolution; like (3.2), these can be calculated effectively by a FFT-based convolution. Since the Fourier transform of the terms $\hat{f}_{eq}(\boldsymbol{l})\phi_{\alpha+\gamma}(\xi_{\boldsymbol{l}}, \theta_p, \varphi_q)$ and $\hat{f}_{eq}(\boldsymbol{m})\psi_\gamma(\xi_{\boldsymbol{m}}, \theta_p, \varphi_q)$ can be precomputed and stored, the computational time required for the linearized collision operator is nearly the same as that for the full BCO. However, for IPL potentials, if $\gamma = (1-\alpha)/2$, the linear gain operator is simplified to

$$\mathscr{L}_g(h) = \iint B(|\boldsymbol{u}|, \theta)[2f_{eq}(\boldsymbol{v}')h(\boldsymbol{v}'_*) - f_{eq}(\boldsymbol{v})h(\boldsymbol{v}_*)]\mathrm{d}\Omega\,\mathrm{d}\boldsymbol{v}_*, \tag{3.7}$$

and its $\boldsymbol{j}$th Fourier mode is approximated by

$$\begin{aligned}\hat{\mathscr{L}}_g(\boldsymbol{j}) \approx\ & \frac{8}{K}\sum_{p,q=1}^{M}\sum_{\substack{\boldsymbol{l}+\boldsymbol{m}=\boldsymbol{j}\\ \boldsymbol{l},\boldsymbol{m}=-N/2}}^{N/2-1} \omega_p\omega_q\hat{f}_{eq}(\boldsymbol{l})\phi_{\alpha+\gamma}(\xi_{\boldsymbol{l}}, \theta_p, \varphi_q)\hat{h}_{\boldsymbol{m}}\psi_\gamma(\xi_{\boldsymbol{m}}, \theta_p, \varphi_q)\sin\theta_p \\ & - \frac{4}{K}\sum_{\substack{\boldsymbol{l}+\boldsymbol{m}=\boldsymbol{j}\\ \boldsymbol{l},\boldsymbol{m}=-N/2}}^{N/2-1} \hat{f}_{eq}(\boldsymbol{l})\hat{h}_{\boldsymbol{m}}\phi_{loss},\end{aligned} \tag{3.8}$$

so the computational cost can be reduced by half.

The symmetry in the VDF can also help to reduce computational cost further. For example, if h is symmetric with respect to v_3, i.e. $h(v_3) = h(-v_3)$, then q in (3.8) can only take values of $1, 2, \ldots, M/2$ for even M. We denote the spectrum obtained in this way as $\hat{\mathscr{L}}_g^z(\boldsymbol{j})$ and let $\mathscr{L}_g^z(\boldsymbol{v}) = \sum_{\boldsymbol{j}} \hat{\mathscr{L}}_g^z(\boldsymbol{j}) \exp(\mathrm{i}\xi_{\boldsymbol{j}} \cdot \boldsymbol{v})$. Then the linear gain operator $\mathscr{L}_g(\boldsymbol{v})$ can be obtained as $\mathscr{L}_g^z(v_1, v_2, v_3) + \mathscr{L}_g^z(v_1, v_2, -v_3)$. In this way the computational cost is reduced by half. This technique can also be applied to the nonlinear BCO.

4. Numerical results for Poiseuille and thermal creep flows using the linearized Boltzmann equation

Poiseuille and thermal creep flows are two classical problems in rarefied gas dynamics. Because of the singular (over-concentration) behaviour in the VDF (Takata & Funagane 2011), the numerical simulation of a highly rarefied gas is a difficult task; for a long time accurate numerical results have been limited to $Kn \leqslant 20$ for a hard-sphere gas (Ohwada, Sone & Aoki 1989; Doi 2010). Recently, some progress has been achieved both analytically and numerically in obtaining the mass and heat flow rates at large Knudsen numbers (Takata & Funagane 2011; Doi 2012*a*,*b*; Funagane & Takata 2012). Here, based on the FSM for the linearized BCO, we solve these two classical flows in parallel plate and rectangular tube configurations up to $Kn \sim 10^6$. The accuracy of the FSM for solving the linearized BE is evaluated by comparing our numerical results for the Poiseuille flow of a hard-sphere gas with those obtained by the numerical kernel method (Ohwada *et al.* 1989). We can then determine the discretization resolutions required in the velocity and frequency spaces, as well as the number of discrete angles M. The influence of the molecular models on the mass and heat flow rates is discussed below; specifically, we check the model accuracy by comparing flow rates for the IPL and LJ models with those for the realistic LJ potentials presented in Sharipov & Bertoldo (2009*b*). Finally, the recent experimental data by Ewart *et al.* (2007) is evaluated.

https://doi.org/10.1017/jfm.2014.79 Published online by Cambridge University Press

4.1. *Poiseuille flow between parallel plates*

Consider a gas between two parallel plates located at $x_2 = -\ell/2$ and $\ell/2$, respectively. A uniform pressure gradient is imposed on the gas in the x_1 direction: the pressure is given by $n_0 k_B T_0(1 + \beta_P x_1/\ell)$ with $|\beta_P| \ll 1$. The BE is linearized around the equilibrium state at rest with number density n_0 and temperature T_0, where the VDF is expressed as $f = f_{eq} + \beta_P(x_1 f_{eq} + h)$. The linearized BE in dimensionless form is then

$$v_2 \frac{\partial h}{\partial x_2} = \mathscr{L}_g(h) - \nu_{eq}(v)h - v_1 f_{eq}, \tag{4.1}$$

and the velocity and heat flux are $V_1 = \int v_1 h \mathrm{d}\boldsymbol{v}$ and $q_1 = \int (|\boldsymbol{v}|^2 - 5/2) v_1 h \mathrm{d}\boldsymbol{v}$, respectively.

Due to symmetry, only half of the spatial region ($-0.5 \leqslant x_2 \leqslant 0$) is simulated, with a specular-reflection boundary condition at $x_2 = 0$. The diffuse boundary condition is adopted at the wall, i.e. $h(x_2 = -0.5, v_2 > 0) = 0$. The spatial domain is divided into N_s non-uniform sections, with most of the discrete points placed near the wall:

$$x_2 = (10 - 15s + 6s^2)s^3 - 0.5, \tag{4.2}$$

where $s = (0, 1, \ldots, N_s)/2N_s$. For $N_s = 100$, the size of the smallest section is 1.24×10^{-6}, while the largest is 0.0094.

Because of the symmetry and smoothness of the VDF, $N_1, N_3 = 12$ uniform grids are used in the $v_1(>0)$ and $v_3(>0)$ directions. The maximum molecular velocity is at $L = 6$. In the discretization of v_2, N_2 non-uniform grids are used:

$$v_2 = \frac{L_2}{(N_2 - 1)^\iota}(-N_2 + 1, -N_2 + 3, \ldots, N_2 - 1)^\iota, \tag{4.3}$$

where $L_2 = 4$ and ι is a positive odd number. Due to the over-concentration in the VDF, large values of N_s and ι should be chosen when investigating large-Kn problems.

The number of frequency components in the ξ_1 and ξ_3 directions are $N_1' \times N_3' = 24 \times 24$, and there are N_2' frequency components in the ξ_2 direction. The FFT is used in the v_1 and v_3 directions, while in the v_2 direction the direct sum is implemented: for non-uniform velocity grids (4.3), we use $\sum_m g(v_{2m}) w_m$ to approximate $\int g(v_2)\mathrm{d}v_2$, where $w_m = \iota L_2 m^{\iota-1}/(N_2 - 1)^\iota$ with $m \in [-N_2 + 1, -N_2 + 3, \ldots, N_2 - 1]$. The resulting overall computational cost is $O(N_2 N_2' N_1' N_3' \ln(N_1' N_3'))$, which is comparable to the FFT-based convolution sum of (3.8).

To obtain the stationary solution, the following implicit iteration scheme is used:

$$\nu_{eq}(v)h^{k+1} + v_2 \frac{\partial h^{k+1}}{\partial x_2} = \mathscr{L}_g(h^k) - v_1 f_{eq}, \tag{4.4}$$

where $\partial h/\partial x_2$ is approximated by a second-order upwind finite difference. The calculation of $\mathscr{L}_g(h^k)$ is as follows: when h^k is known, we obtain $\hat{\mathscr{L}}_g$ from (3.8). Then we obtain $\mathscr{L}_g(h^k)$ by applying the inverse FFT to $\hat{\mathscr{L}}_g$: $\mathscr{L}_g(h^k) = \sum_{j=-N/2}^{N/2-1} \hat{\mathscr{L}}_g(j) \exp(\mathrm{i}\xi_j \cdot \boldsymbol{v})$. The iterations are terminated when changes in the mass flow rate

$$\mathscr{M} = 2\int_{-1/2}^{0} V_1 \mathrm{d}x_2, \tag{4.5}$$

https://doi.org/10.1017/jfm.2014.79 Published online by Cambridge University Press

and heat flow rate

$$\mathscr{Q} = 2\int_{-1/2}^{0} q_1 \mathrm{d}x_2, \tag{4.6}$$

between two consecutive iteration steps are less than 10^{-8}.

To validate the FSM for the linearized BE, our numerical results are compared to those obtained using the numerical kernel method (Ohwada *et al.* 1989) for a hard-sphere gas ($\omega = 0.5$). For $k = 8Kn/5\sqrt{\pi} \leqslant 20$, the number of equispaced frequency components is $N_2' = 32$ and the velocity discretization is given by (4.3) with $N_2 = 48$ and $\iota = 3$. For $k \geqslant 100$, we choose $N_2' = 64$, $N_2 = 100$, and $\iota = 7$. The comparisons are summarized in table 1. It is seen that, when we use $M = 6$, the relative error in the mass flow rate between the two methods is less than 0.1 %, while that in the heat flow rate is less than 0.25 %. When $M = 8$ (or 12), a relative error less than 0.01 % can be achieved. Our method produces accurate results even when the Knudsen number is very large. We also compared our numerical results with those from the information-preserving DSMC (Fan & Shen 2001), and found that the information-preserving method works well except at extremely large Knudsen number: the relative error in the mass flow rate between the two methods reaches ∼7 % at $Kn_{vhs} = 100$.

We now compare the mass and heat flow rates for a hard-sphere gas ($\omega = 0.5$), for argon ($\omega = 0.81$), and for a Maxwell gas ($\omega = 1$) using the IPL models. The numerical

	Fast spectral method						Literature	
	$M = 6$		$M = 8$		$M = 12$			
k	$-\mathscr{M}$	$\mathscr{Q}$	$-\mathscr{M}$	$\mathscr{Q}$	$-\mathscr{M}$	$\mathscr{Q}$	$-\mathscr{M}$	$\mathscr{Q}$
0.1	1.1951	0.0550	1.1953	0.0551	1.1953	0.0552	1.1930	0.0553
0.15	0.9948	0.0758	0.9946	0.0760	0.9947	0.0760	0.9938	0.0761
0.2	0.9006	0.0931	0.9003	0.0934	0.9004	0.0934	0.8999	0.0935
0.3	0.8156	0.1205	0.8154	0.1208	0.8154	0.1208	0.8152	0.1209
0.4	0.7804	0.1415	0.7802	0.1418	0.7802	0.1418	0.7801	0.1419
0.6	0.7566	0.1727	0.7563	0.1729	0.7563	0.1729	0.7562	0.1730
0.8	0.7537	0.1957	0.7534	0.1958	0.7533	0.1759	0.7533	0.1958
1	0.7580	0.2139	0.7576	0.2139	0.7575	0.2138	0.7574	0.2140
1.5	0.7778	0.2479	0.7774	0.2478	0.7771	0.2475	0.7771	0.2477
2	0.7998	0.2726	0.7994	0.2725	0.7991	0.2722	0.7991	0.2724
3	0.8405	0.3085	0.8402	0.3084	0.8398	0.3079	0.8398	0.3082
4	0.8755	0.3348	0.8753	0.3348	0.8749	0.3342	0.8749	0.3345
6	0.9326	0.3731	0.9325	0.3733	0.9321	0.3727	0.9321	0.3730
8	0.9781	0.4013	0.9781	0.4016	0.9777	0.4011	0.9778	0.4015
10	1.0161	0.4239	1.0161	0.4243	1.0158	0.4238	1.0159	0.4242
15	1.0907	0.4664	1.0908	0.4669	1.0905	0.4664	1.0908	0.4669
20	1.1475	0.4977	1.1477	0.4982	1.1475	0.4978	1.1479	0.4984
10^2	1.5139	0.6897	1.5141	0.6898	1.5142	0.6900	1.5143	0.6900
10^3	2.1208	0.9959	2.1209	0.9959	2.1210	0.9960	2.1210	0.9960
10^4	2.7614	1.3165	2.7614	1.3165	2.7615	1.3165	2.7615	1.3166
10^5	3.4094	1.6406	3.4094	1.6405	3.4094	1.6405	3.4094	1.6406
10^6	4.0586	1.9653	4.0587	1.9652	4.0587	1.9652	4.0587	1.9652

TABLE 1. Mass and heat flow rates in Poiseuille flow between parallel plates of a hard-sphere gas. For $k = 8Kn/5\sqrt{\pi} \leqslant 20$ and $k \geqslant 10^2$, the data in the last two columns are collected from Ohwada *et al.* (1989) and Takata & Funagane (2011), respectively.

https://doi.org/10.1017/jfm.2014.79 Published online by Cambridge University Press

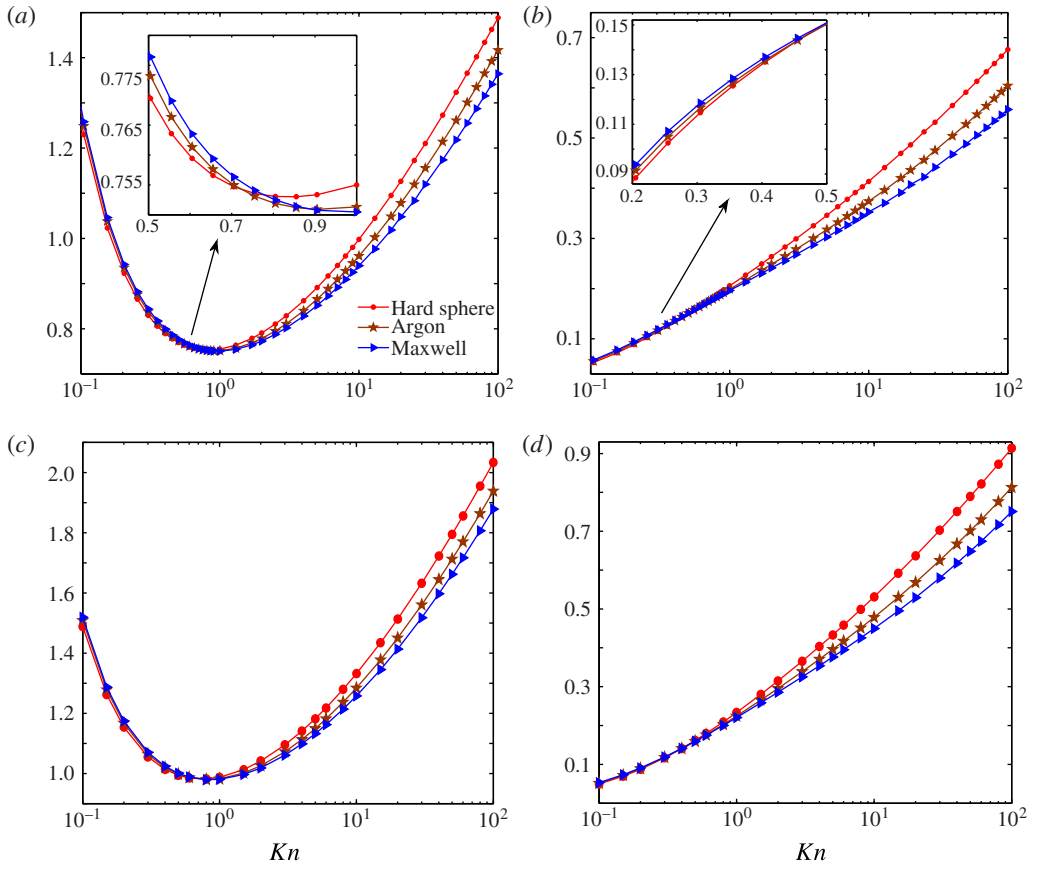


FIGURE 1. (Colour online) Comparisons of mass and heat flow rates for different IPL molecular models in Poiseuille gas flow between parallel plates. (*a*) Mass flow rate $-\mathscr{M}$ and (*b*) heat flow rate $\mathscr{Q}$, at $\alpha_a = 1.0$; (*c*) $-\mathscr{M}$ and (*d*) $\mathscr{Q}$, at $\alpha_a = 0.8$. Here α_a represents the wall accommodation coefficient, where the boundary condition at $x_2 = -0.5$ is $h(v_1, v_2, v_3, x_2 = -0.5) = (1 - \alpha_a)h(v_1, -v_2, v_3, x_2 = -0.5)$ for $v_2 > 0$.

results are shown in figure 1. We denote as Kn_c (≈ 0.9) the Knudsen number at which there is the Knudsen minimum in the mass flow rate. When $Kn > Kn_c$ (or $Kn < Kn_c$), the mass flow rate decreases (or increases) as the viscosity index ω increases, for a fixed value of Kn. For instance, at $Kn = 10$, the mass flow rate of the Maxwell gas is $\sim 94\,\%$ that of the hard-sphere gas when $\alpha_a = 1$. The underlying mechanism for this may be understood in terms of the effective collision frequency: for the same value of shear viscosity, the average collision frequency $\int \nu_{eq}(v) f_{eq} \mathrm{d}v / \int f_{eq} \mathrm{d}v$ increases with ω (see figures 12 and 13 in Wu *et al.* 2013 and the corresponding text therein). Therefore, Maxwell molecules have a greater effective collision frequency (and a smaller effective Kn) than hard-sphere molecules. Since at large Kn the mass flow rate increases with Kn, the Maxwell gas has a lower mass flow rate than the hard-sphere gas. Conversely, since at small Kn the mass flow rate decreases with Kn, when $Kn < Kn_c$, the Maxwell gas has a higher mass flow rate than the hard-sphere gas, although the difference is very small. The heat flow rate behaves similarly to the mass flow rate; that is, when $Kn > 0.5$ (or $Kn < 0.5$), the heat flow rate decreases (or increases) as ω increases, for a fixed value of Kn. The difference in flow rates

https://doi.org/10.1017/jfm.2014.79 Published online by Cambridge University Press

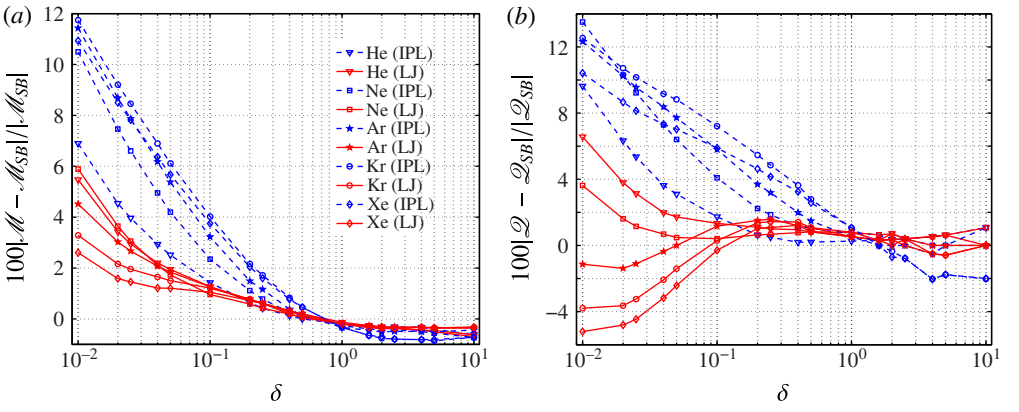


FIGURE 2. (Colour online) Relative differences in (*a*) the mass and (*b*) heat flow rates between the molecular models and LJ potentials in Poiseuille gas flow between parallel plates for various δ. The subscripts SB indicate the results from Sharipov & Bertoldo (2009*b*).

between various gases with the same value of shear viscosity holds when the wall accommodation coefficient α_a is not 1, see figure 1(*c*,*d*).

Since IPL potentials are simplifications of the realistic LJ potential, it is interesting to check the accuracy of the collision kernels (2.3) and (2.7). Tables 2 and 3 compare the mass flow rates and heat flow rates for five noble gases with the data of Sharipov & Bertoldo (2009*b*) for the LJ potential. For the IPL models, at a temperature of 300 K, we use the viscosity index $\omega_{He} = \omega_{Ne} = 0.66$ (so only the results for helium are shown), $\omega_{Ar} = 0.81 \simeq \omega_{Kr} = 0.80$ (so only the results for argon are shown), and $\omega_{Xe} = 0.85$. For the LJ potential, the potential depth ϵ of He, Ne, Ar, Kr, and Xe is $10.22k_B$, $35.7k_B$, $124k_B$, $190k_B$, and $229k_B$, respectively. The relative differences between the mass and heat flow rates produced by the FSM and those in Sharipov & Bertoldo (2009*b*) are visualized in figure 2. For $\delta > 0.2$, the relative difference $|\mathscr{M}_{IPL} - \mathscr{M}_{SB}|/|\mathscr{M}_{SB}|$ between the IPL models and LJ potentials is less than 1 %. For $\delta < 0.2$, the relative difference increases as δ decreases. Specifically, at $\delta = 0.01$, the IPL model overestimates the mass flow rate by around 6.9 %, 10.5 %, 11.4 %, 11.7 %, and 11.0 % for He, Ne, Ar, Kr, and Xe, respectively. When the collision kernel (2.7) is used for the LJ potential, at $\delta = 0.01$, the LJ model overestimates the mass flow rate by around 5.5 %, 6.0 %, 4.5 %, 3.3 %, and 2.6 % for He, Ne, Ar, Kr, and Xe, respectively. As δ increases, the relative difference quickly decreases. Similar behaviour can be observed for the heat flow rate, except that the LJ models for Ar, Kr, and Xe underestimate the heat flow rate at small values of δ. Generally speaking, when compared to the solution for the realistic LJ potential, the LJ model yields closer results than the IPL model.

4.2. *Thermal creep flow between parallel plates*

In thermal creep flow, the wall temperature varies as $T = T_0(1 + \beta_T x_1/\ell)$, where $|\beta_T| \ll 1$. The VDF is expressed as $f = f_{eq} + \beta_T[x_1 f_{eq}(|\boldsymbol{v}|^2 - 5/2) + h]$ and the linearized BE is given by (4.1) with the last term replaced by $v_1(|\boldsymbol{v}|^2 - 5/2)f_{eq}$.

The Onsager–Casimir relation (Loyalka 1971; Sharipov 1994*a*,*b*; Takata 2009*a*,*b*) states that the mass flow rate in thermal creep flow is equal to the heat flow rate in Poiseuille flow: $\int V_1[h_T]\mathrm{d}x_2 = \int q_1[h_P]\mathrm{d}x_2$. Recently, Takata & Funagane (2011)

https://doi.org/10.1017/jfm.2014.79 Published online by Cambridge University Press

https://doi.org/10.1017/jfm.2014.79 Published online by Cambridge University Press

	He			Ne		Ar			Kr		Xe		
δ	IPL FSM	LJ FSM	LJ SB	LJ FSM	LJ SB	IPL FSM	LJ FSM	LJ SB	LJ FSM	LJ SB	IPL FSM	LJ FSM	LJ SB
0.010	2.852	2.814	2.668	2.733	2.581	2.788	2.615	2.502	2.577	2.495	2.770	2.562	2.497
0.020	2.534	2.507	2.424	2.444	2.358	2.478	2.349	2.280	2.318	2.269	2.463	2.306	2.270
0.025	2.438	2.414	2.345	2.357	2.287	2.385	2.270	2.211	2.242	2.199	2.371	2.231	2.199
0.040	2.246	2.230	2.182	2.185	2.140	2.200	2.115	2.072	2.092	2.058	2.188	2.082	2.057
0.050	2.160	2.148	2.107	2.109	2.073	2.117	2.046	2.009	2.025	1.995	2.106	2.017	1.993
0.100	1.920	1.917	1.893	1.894	1.876	1.889	1.853	1.830	1.838	1.816	1.881	1.832	1.813
0.200	1.726	1.728	1.715	1.717	1.707	1.704	1.691	1.679	1.681	1.668	1.699	1.677	1.665
0.250	1.674	1.677	1.667	1.668	1.661	1.656	1.647	1.637	1.638	1.628	1.651	1.635	1.625
0.400	1.584	1.587	1.582	1.583	1.580	1.572	1.569	1.566	1.564	1.559	1.569	1.561	1.557
0.500	1.552	1.555	1.552	1.551	1.550	1.542	1.541	1.540	1.537	1.535	1.540	1.536	1.533
1.000	1.504	1.505	1.507	1.505	1.508	1.502	1.504	1.507	1.504	1.507	1.502	1.504	1.507
1.600	1.530	1.530	1.534	1.531	1.536	1.533	1.536	1.540	1.538	1.543	1.534	1.539	1.544
2.000	1.565	1.565	1.570	1.566	1.572	1.570	1.573	1.578	1.576	1.582	1.572	1.578	1.583
2.500	1.619	1.618	1.624	1.620	1.626	1.626	1.629	1.634	1.633	1.639	1.628	1.635	1.641
4.000	1.813	1.811	1.819	1.814	1.822	1.824	1.827	1.833	1.833	1.839	1.827	1.836	1.842
5.000	1.955	1.953	1.963	1.957	1.966	1.968	1.971	1.978	1.978	1.985	1.972	1.981	1.988
10.00	2.723	2.721	2.740	2.726	2.743	2.744	2.746	2.756	2.755	2.764	2.748	2.759	2.768

TABLE 2. Mass flow rate ($-2\mathscr{M}$) in Poiseuille flow of various gases between parallel plates for various δ, see (2.6). The data in columns denoted by SB are those results from Sharipov & Bertoldo (2009*b*).

https://doi.org/10.1017/jfm.2014.79 Published online by Cambridge University Press

	He			Ne		Ar			Kr		Xe		
δ	IPL FSM	LJ FSM	LJ SB	LJ FSM	LJ SB	IPL FSM	LJ FSM	LJ SB	LJ FSM	LJ SB	IPL FSM	LJ FSM	LJ SB
0.010	1.252	1.217	1.142	1.143	1.103	1.185	1.043	1.055	1.013	1.053	1.166	1.001	1.056
0.020	1.092	1.066	1.027	1.006	0.990	1.033	0.924	0.937	0.899	0.933	1.016	0.890	0.935
0.025	1.042	1.020	0.989	0.965	0.954	0.986	0.890	0.900	0.866	0.895	0.970	0.857	0.897
0.040	0.942	0.927	0.909	0.884	0.878	0.893	0.821	0.824	0.801	0.818	0.879	0.793	0.819
0.050	0.897	0.885	0.870	0.847	0.843	0.851	0.790	0.790	0.771	0.782	0.838	0.764	0.783
0.100	0.764	0.761	0.751	0.737	0.734	0.729	0.697	0.689	0.682	0.680	0.719	0.677	0.679
0.200	0.641	0.644	0.637	0.631	0.627	0.617	0.604	0.595	0.593	0.585	0.610	0.589	0.583
0.250	0.604	0.607	0.601	0.597	0.593	0.583	0.574	0.565	0.564	0.556	0.577	0.560	0.554
0.400	0.527	0.531	0.526	0.525	0.521	0.513	0.509	0.503	0.502	0.495	0.509	0.499	0.493
0.500	0.492	0.495	0.491	0.491	0.487	0.480	0.477	0.473	0.473	0.467	0.477	0.470	0.465
1.000	0.386	0.387	0.385	0.386	0.383	0.381	0.381	0.379	0.379	0.377	0.380	0.379	0.376
1.600	0.316	0.316	0.315	0.316	0.314	0.315	0.316	0.315	0.316	0.315	0.315	0.316	0.315
2.000	0.283	0.284	0.282	0.284	0.282	0.284	0.285	0.284	0.286	0.285	0.284	0.286	0.286
2.500	0.252	0.252	0.251	0.252	0.251	0.254	0.255	0.254	0.256	0.256	0.254	0.257	0.256
4.000	0.189	0.189	0.188	0.190	0.189	0.192	0.193	0.193	0.195	0.196	0.193	0.196	0.197
5.000	0.162	0.162	0.161	0.163	0.162	0.166	0.166	0.166	0.168	0.169	0.167	0.169	0.170
10.00	0.094	0.093	0.093	0.094	0.093	0.097	0.097	0.097	0.099	0.099	0.098	0.100	0.100

TABLE 3. Heat flow rate ($2\mathscr{Q}$) in Poiseuille flow of various gases between parallel plates for various δ. The data in columns denoted by SB are those results from Sharipov & Bertoldo (2009*b*).

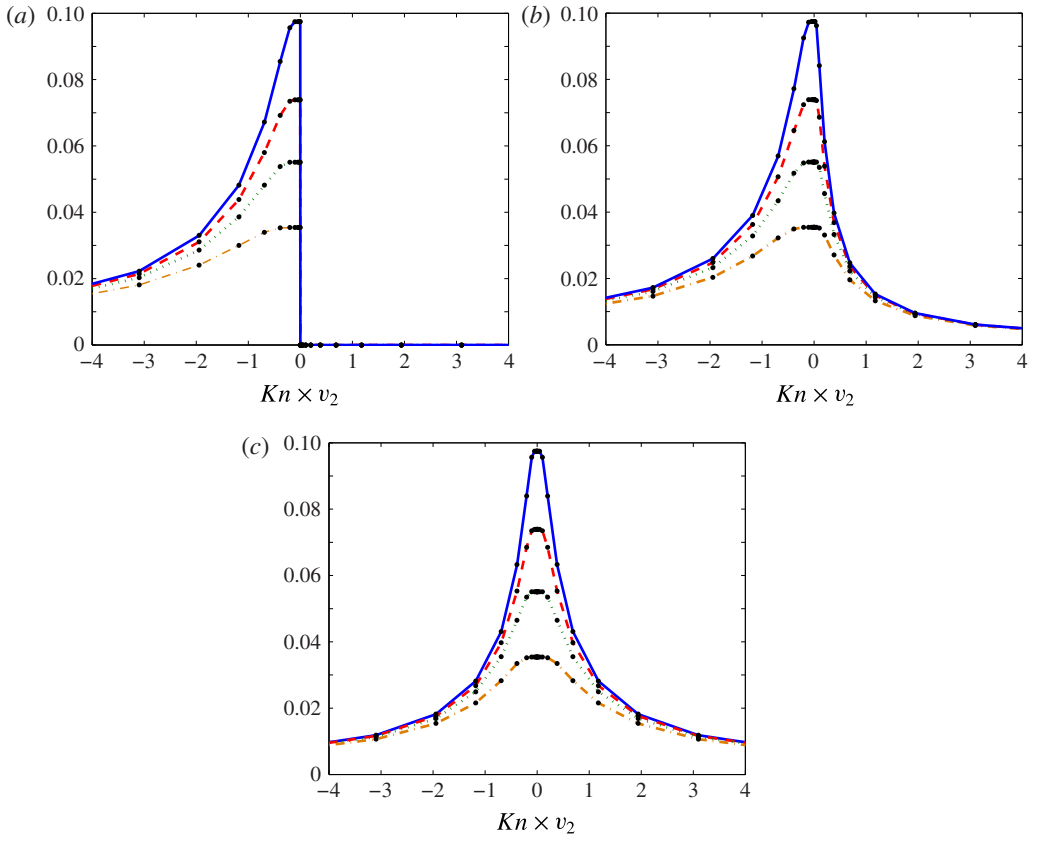


FIGURE 3. (Colour online) Demonstration of a strong Onsager–Casimir relation at the microscopic level. Lines (or dots): velocity distribution functions $(|v|^2 - 5/2)h_P$ in Poiseuille flow (or h_T in thermal creep flow) at v_1, $v_3 = 6/31$ and $Kn = 10^4$. The curves correspond to, from top to bottom the hard-sphere, helium (IPL), argon (IPL), and Maxwell gases, respectively. (*a*) $x_2 = -0.5$, (*b*) $x_2 = -0.25$, (*c*) $x_2 = 0$.

observed a strong relation, that is, at large Kn, $V_1[h_T]$ and $q_1[h_P]$ have identical spatial profiles, i.e. $V_1[h_T] = q_1[h_P] + O[Kn^{-1}(\ln Kn)^2]$. The VDFs obtained by our FSM in figure 3 show that a stronger Onsager–Casimir relation exists at the microscopic level, that is, $h_T \approx (|\boldsymbol{v}|^2 - 5/2)h_P$, at large Kn, for various IPL models.

Because of the Onsager–Casimir relation, we compare only the heat flow rates in thermal creep flow for different potential models. The results are in table 4. For a particular molecular model, the heat flow rate increase monotonically as δ decreases. As in the Poiseuille flow case, different molecular models have different flow rates at the same value of shear viscosity; for IPL models, the heat flow rate always decreases as ω increases.

The relative difference in heat flow rates is visualized in figure 4. At $\delta = 0.01$, for He, Ne, Ar, Kr, and Xe, the IPL models overestimate the heat flow rate relative to Sharipov & Bertoldo (2009*b*) by 6.6 %, 10.3 %, 11.4 %, 11.7 %, and 11 %, while the LJ model overestimates the heat flow rate by 5.1 %, 5.7 %, 4.6 %, 3.5 %, and 2.9 %, respectively. As δ increases, the relative difference quickly decreases. This comparison, together with those for Poiseuille flows, indicate that, in the free-molecular regime, it is necessary to consider the LJ potential to get highly reliable results (Sharipov

https://doi.org/10.1017/jfm.2014.79 Published online by Cambridge University Press

https://doi.org/10.1017/jfm.2014.79 Published online by Cambridge University Press

	He			Ne		Ar			Kr		Xe		
δ	IPL FSM	LJ FSM	LJ SB	LJ FSM	LJ SB	IPL FSM	LJ FSM	LJ SB	LJ FSM	LJ SB	IPL FSM	LJ FSM	LJ SB
0.010	6.269	6.182	5.879	6.010	5.684	6.140	5.768	5.512	5.691	5.496	6.104	5.662	5.500
0.020	5.496	5.435	5.263	5.301	5.121	5.385	5.109	4.958	5.048	4.934	5.354	5.024	4.935
0.025	5.255	5.202	5.059	5.082	4.936	5.151	4.906	4.779	4.850	4.754	5.121	4.828	4.754
0.040	4.761	4.725	4.626	4.632	4.542	4.670	4.491	4.404	4.445	4.376	4.644	4.427	4.373
0.050	4.532	4.505	4.421	4.424	4.353	4.448	4.298	4.225	4.257	4.197	4.424	4.240	4.193
0.100	3.848	3.840	3.792	3.793	3.761	3.784	3.709	3.669	3.679	3.641	3.766	3.666	3.635
0.200	3.196	3.200	3.174	3.175	3.162	3.151	3.120	3.103	3.098	3.080	3.138	3.089	3.074
0.250	2.992	2.997	2.977	2.977	2.968	2.951	2.929	2.918	2.909	2.897	2.940	2.901	2.891
0.400	2.569	2.575	2.562	2.562	2.560	2.538	2.526	2.525	2.511	2.508	2.529	2.504	2.502
0.500	2.371	2.377	2.367	2.367	2.366	2.343	2.335	2.337	2.321	2.322	2.336	2.316	2.317
1.000	1.772	1.776	1.770	1.770	1.771	1.752	1.750	1.756	1.741	1.745	1.748	1.737	1.741
1.600	1.387	1.391	1.385	1.387	1.387	1.373	1.371	1.377	1.365	1.369	1.369	1.362	1.366
2.000	1.216	1.219	1.213	1.215	1.216	1.203	1.202	1.207	1.197	1.201	1.200	1.194	1.198
2.500	1.054	1.057	1.051	1.054	1.053	1.043	1.042	1.046	1.038	1.041	1.040	1.036	1.039
4.000	0.752	0.754	0.750	0.752	0.752	0.745	0.745	0.747	0.742	0.744	0.743	0.740	0.743
5.000	0.631	0.633	0.629	0.631	0.630	0.625	0.625	0.627	0.622	0.625	0.623	0.621	0.624
10.00	0.347	0.348	0.345	0.347	0.346	0.344	0.344	0.345	0.343	0.344	0.343	0.342	0.344

TABLE 4. Heat flow rate ($2\mathcal{Q}$) in thermal creep flow of various gases between parallel plates for various δ. The data in columns denoted by SB are those results from Sharipov & Bertoldo (2009*b*).

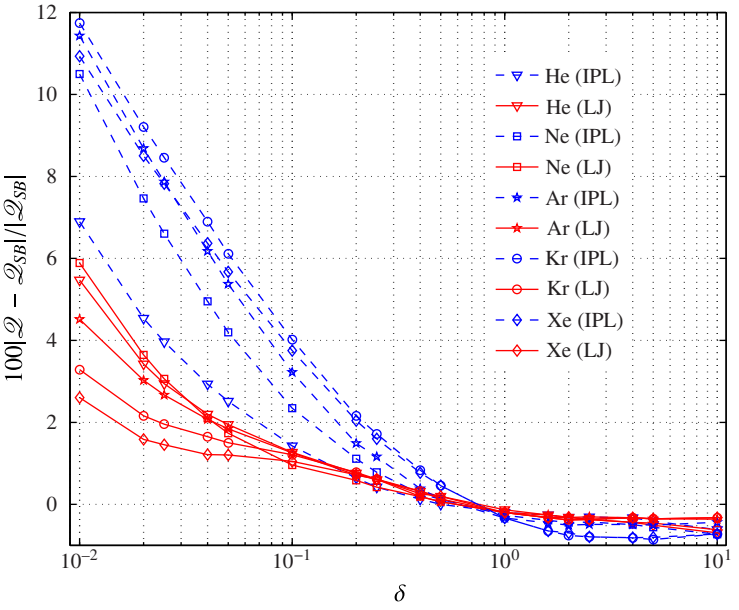


FIGURE 4. (Colour online) Relative difference in the heat flow rate between different molecular models and the LJ potential in thermal creep flow between parallel plates as a function of δ.

& Strapasson 2012; Venkattraman & Alexeenko 2012; Sharipov & Strapasson 2013). However, the LJ model with the collision kernel (2.7) can produce mass and heat flow rates with a relative error less than 2 % when $\delta > 0.04$ or, equivalently, $Kn < 22$.

In the free-molecular limit, it has previously been found that the mass flow rates in Poiseuille and thermal creep flows increase logarithmically with the Knudsen number (Cercignani & Daneri 1963; Takata & Funagane 2011). Our numerical results show that the heat flow rate in thermal creep flow can also be fitted to a logarithmic function of Kn, namely $\mathscr{Q}[h_T] = -0.6345\ \ln(Kn) - \mathscr{Q}_0$ in the region $10^5 < Kn < 2 \times 10^6$, where the constant $\mathscr{Q}_0$ is 0.2679, 0.1762, 0.07371, and -0.09903 for hard-sphere, helium, argon, and the Maxwell gases when the IPL model is used, respectively.

4.3. *Poiseuille and thermal creep flow along a rectangular tube*

We now consider rarefied gases in a long straight tube that lies along the x_3 axis. The cross-section is uniform and rectangular, so that $-A\ell/2 < x_1 < A\ell/2$ and $-\ell/2 < x_2 < \ell/2$, where A is the aspect ratio. The linearized BE in dimensionless form for Poiseuille flow along this rectangular tube is

$$v_1 \frac{\partial h}{\partial x_1} + v_2 \frac{\partial h}{\partial x_2} = \mathscr{L}_g(h) - \nu_{eq}(v)h - v_3 f_{eq}, \tag{4.7}$$

while v_3 should be replaced by $v_3\left(|\boldsymbol{v}|^2 - 5/2\right)$ for a thermal creep flow. Due to symmetry, only one quarter of the spatial domain is considered. The mass flow rate is defined as $\mathscr{M} = (4/A)\int_{-1/2}^{0}\int_{-A/2}^{0} V_3 \mathrm{d}x_1\mathrm{d}x_2$ and the heat flow rate is $\mathscr{Q} = (4/A)\int_{-1/2}^{0}\int_{-A/2}^{0} q_3 \mathrm{d}x_1\mathrm{d}x_2$, where $V_3 = \int v_3 h \mathrm{d}\boldsymbol{v}$ and $q_3 = \int \left(|\boldsymbol{v}|^2 - 5/2\right) v_3 h \mathrm{d}\boldsymbol{v}$.

https://doi.org/10.1017/jfm.2014.79 Published online by Cambridge University Press

This problem was first solved for a hard-sphere gas by the numerical kernel method (Doi 2010) and then by the low-noise DSMC method (Radtke *et al.* 2011). To compare the numerical accuracy and efficiency of our new FSM, we first consider the thermal creep flow at $Kn_{vhs} = 0.1$ and $A = 2$. We use a 50×50 non-uniform spatial grid (see (4.2)), 32×32 non-uniform velocity grids ((4.3) with $\iota = 3$) in the v_1 and v_2 directions, and 12 uniform mesh points in the v_3 direction. The FSM with $M = 6$ yields $\mathscr{M} = 0.0478$, compared to 0.048 by Doi (2010) and 0.0473 by Radtke *et al.* (2011). We then consider Poiseuille flow in the square tube; with a 25×25 spatial cell mesh, $32 \times 32 \times 24$ frequency components, and $M = 6$, we obtain $\mathscr{M} = 0.3808$ and 0.3966, $\mathscr{Q} = 0.1365$ and 0.1874 for $Kn_{vhs} = 1$ and 10, respectively, compared to Doi's 0.381 and 0.396 for $\mathscr{M}$, and 0.136 and 0.187 for $\mathscr{Q}$. The computational time is 100 and 40 s, respectively (our Fortran program runs on a computer with an Intel Xeon 3.3 GHz CPU, and only one core is used), compared to the low-noise DSMC that takes 66 and 12 min , respectively. (This DSMC code runs on a single core of an Intel Q9650, 3.0 GHz Core 2 Quad processor. The time is obtained when there is better than 0.1 % statistical uncertainty in the mass flow rate. To achieve the same level of uncertainty in the velocity field, the low-noise DSMC would need 240 and 120 min, respectively). These comparisons indicate that the FSM is both accurate and efficient new numerical method.

We observe that the difference in mass and heat flow rates between different molecular models is very small when $A = 1$. Although the difference increases with A, at $A = 10$, $|(\mathscr{M}_{Ar} - \mathscr{M}_{He})/\mathscr{M}_{Ar}|$ is only 1.6 % at $\delta = 0.01$, while that at $A = \infty$ is 7.6 %, when the LJ model is used. So, in the following numerical simulation we only use the IPL model.

We now compare our numerical results with recent experiments on the reduced mass flow rate in Poiseuille flow (Ewart *et al.* 2007). The tube cross-section is rectangular, with an aspect ratio of $A = 52.45$. The working gas is helium and we take the IPL model with $\omega = 0.66$. In the spatial discretization, 100 and 50 non-uniform grid points are used in the x_1 and x_2 directions, respectively. The number of velocity grids is $32 \times 32 \times 12$, the frequency components are $32 \times 32 \times 24$, and the number of discrete angles is $M = 6$. Different wall accommodation coefficients α_a are used: the wall boundary condition is given by $h(v_1, v_2, v_3, x_1 = -A/2, x_2) = (1 - \alpha_a)h(-v_1, v_2, v_3, x_1 = -A/2, x_2)$ for $v_1 > 0$ and $h(v_1, v_2, v_3, x_1, x_2 = -1/2) = (1 - \alpha_a)h(v_1, -v_2, v_3, x_1, x_2 = -1/2)$ for $v_2 > 0$. The obtained mass flow rate $\mathscr{M}$ is transformed to the reduced mass flow rate G via the following equation (Sharipov & Seleznev 1994):

$$G(\delta_{in}, \delta_{out}) = \frac{2}{\delta_{out} - \delta_{in}} \int_{\delta_{in}}^{\delta_{out}} \mathscr{M}(\delta) \mathrm{d}\delta, \tag{4.8}$$

where the subscripts '*in*' and '*out*' stand for the inlet and outlet, respectively. The reduced mass flow rate G no longer depends on the local pressure gradient, but only on the mean value of pressure; so the parameter δ_m at the mean pressure of the tube is also introduced. We consider the published experimental data where the inlet to outlet pressure ratio is 5, so that $\delta_{in} = 5\delta_m/3$ and $\delta_{out} = \delta_m/3$. The mass flow rate $\mathscr{M}$ is obtained at discrete values of the rarefaction parameter. The reduced mass flow rate is calculated by (4.8), where $\mathscr{M}$ at an unknown δ is obtained by cubic interpolation. Comparisons between the numerical and experimental data are visualized in figure 5. When $\delta \geqslant 6$, the experimental data agree well with the numerical results from the BE if $\alpha_a = 0.92$. In the region $1 \leqslant \delta < 6$, the experimental data agree with the numerical results if $\alpha_a = 0.92 \sim 1$. For $0.2 \leqslant \delta \leqslant 1$, the mass flow rates from the BE with $\alpha_a = 0.92$ agree with the experimental measurements. When $\delta \leqslant 0.1$, the BE with $\alpha_a = 0.95 \sim 1$ agrees well with the experimental results.

https://doi.org/10.1017/jfm.2014.79 Published online by Cambridge University Press

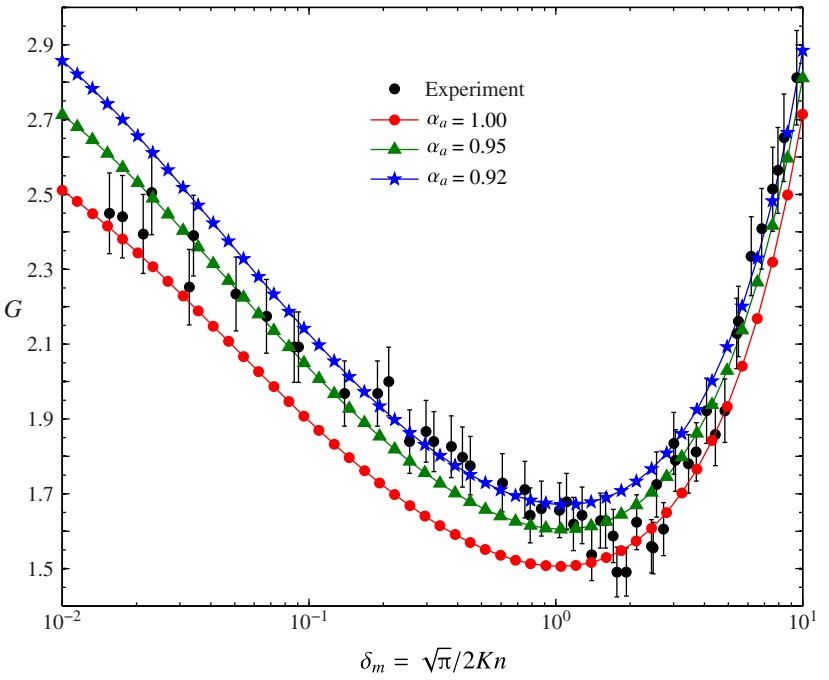


FIGURE 5. (Colour online) Comparison of the FSM-calculated reduced mass flow rate G in Poiseuille flow along a rectangular tube (aspect ratio 52.45) with the experimental data of Ewart *et al.* (2007), for various values of the wall accommodation coefficient α_a.

Note that the advantage of the FSM over the DSMC method becomes more profound for a series of simulations with the same spatial geometry but different values of Kn. Sorting Kn in descending order, the converged VDF at the previous Kn can be used as the initial condition for the FSM for those subsequent Kn. In this way, the computational efficiency can be improved further. For example, for this Poiseuille flow problem, it takes 4.4 h to compute the solution for $Kn = 0.1$ when the initial VDF is the global equilibrium one, but only 2 h when the initial VDF is taken as the solution at $Kn = 0.15$.

5. Numerical results for the nonlinear Boltzmann equation

In this section, a number of two-dimensional simulations using the nonlinear BE are carried out in the transition flow regime ($0.1 \leqslant Kn \leqslant 10$) and the free-molecular regime using the IPL models. The influence of the IPL models on the macroscopic flow properties is assessed, and the applicability of the linear BCO for microflows with large temperature variations is evaluated. A linear scaling law is proposed for the flow velocities in thermally driven flows in the free-molecular regime. Specifically, thermal creep flow inside a closed channel is analysed, where the flow pattern can be well explained as the superposition of both the velocity profiles of linearized Poiseuille and thermal creep flow between parallel plates.

5.1. *Lid-driven cavity flow*

Consider the lid-driven flow in a square cavity, as has been previously studied using DSMC (John, Gu & Emerson 2010, 2011). Since the gas velocity near the lower

https://doi.org/10.1017/jfm.2014.79 Published online by Cambridge University Press

wall is small, the DSMC solution is extremely time-consuming. Even when the velocity of the moving upper lid is so small that the linearized BE can be applied, the low-noise DSMC method (Radtke *et al.* 2011) takes more than 1 day to achieve reasonably resolved results at $Kn_{vhs} = 0.1$.

We solve this problem (for argon gas, an upper lid velocity of 50 m s^{-1}, and a wall temperature of 273 K) in a 51×51 non-uniform spatial grid, see (4.2). The minimum length of the spatial cell is 7.8×10^{-5}, while the maximum is 0.0375, with most of the grid points located near the walls. For $Kn_{vhs} = 0.1$ and 1, $32 \times 32 \times 12$ grid points in velocity space are used, while for $Kn_{vhs} = 10$, there are $64 \times 64 \times 12$ velocity grid points, with most of the grid points located in $v_1, v_2 \sim 0$ to capture the discontinuities in the VDF. The number of frequency components is $32 \times 32 \times 24$. The BCO is approximated by the FSM with $M = 6$, and the spatial derivatives are approximated by second-order upwind finite differences. We solve the discretized BE by the implicit scheme in an iterative manner. At the $(k + 1)$th iteration step, the VDF at the wall (entering the cavity) is determined according to the diffuse boundary condition, using the VDF at the same position (but leaving the cavity) at the previous iteration step. This numerical scheme is much faster than an explicit time-dependent technique because no Courant–Friedrichs-Lewy condition is imposed (Frangi, Ghisi & Frezzotti 2007). However, the disadvantage is that, when the mass flux entering the cavity at the $(k+1)$th step (which is equal to that leaving the cavity at the kth step) is not equal to that leaving the cavity at the $(k + 1)$th step, the total mass inside the cavity is not conserved. To overcome this, at the end of each iteration step, a simple correction of the VDF by a factor equal to the initial total mass divided by the current total mass is introduced. This is sufficient to recover the correct steady-state conditions, and was introduced by Mieussens & Struchtrup (2004).

The convergence rate of our iterative scheme is proportional to the Knudsen number. For $Kn_{vhs} = 0.1$ and 1, starting from the global equilibrium state, the FSM takes 110 and 14 min, respectively, to produce a converged solution, which is when the error between two consecutive iteration steps,

$$\|\epsilon\|_2 = \max\left\{\sqrt{\frac{\int |V_1^{k+1} - V_1^k|^2 \mathrm{d}x_1\mathrm{d}x_2}{\int |V_1^k|^2 \mathrm{d}x_1\mathrm{d}x_2}}, \sqrt{\frac{\int |V_2^{k+1} - V_2^k|^2 \mathrm{d}x_1\mathrm{d}x_2}{\int |V_2^k|^2 \mathrm{d}x_1\mathrm{d}x_2}}\right\}, \tag{5.1}$$

is less than 10^{-5}.

Figure 6 shows the calculated temperature contours and streamlines in the lid-driven cavity flow of argon gas with diffuse boundary conditions. Compared to DSMC, these solutions are free of noise. We have also simulated the flow of a hard-sphere gas, with the same values of the normalized wall velocity (i.e. 0.148) and shear viscosity (the Knudsen numbers Kn are the same, but the Kn_{vhs} are different). Comparisons of the velocity, temperature, and heat flux profiles between the two IPL molecular models are shown in figure 7, and demonstrate that the molecular model has little influence on the flow pattern. This may explain why, for the same problem, the Bhatnagar–Gross–Krook (BGK) and Shakhov kinetic models can both produce excellent results that are in agreement with DSMC data (Huang, Xu & Yu 2012).

https://doi.org/10.1017/jfm.2014.79 Published online by Cambridge University Press

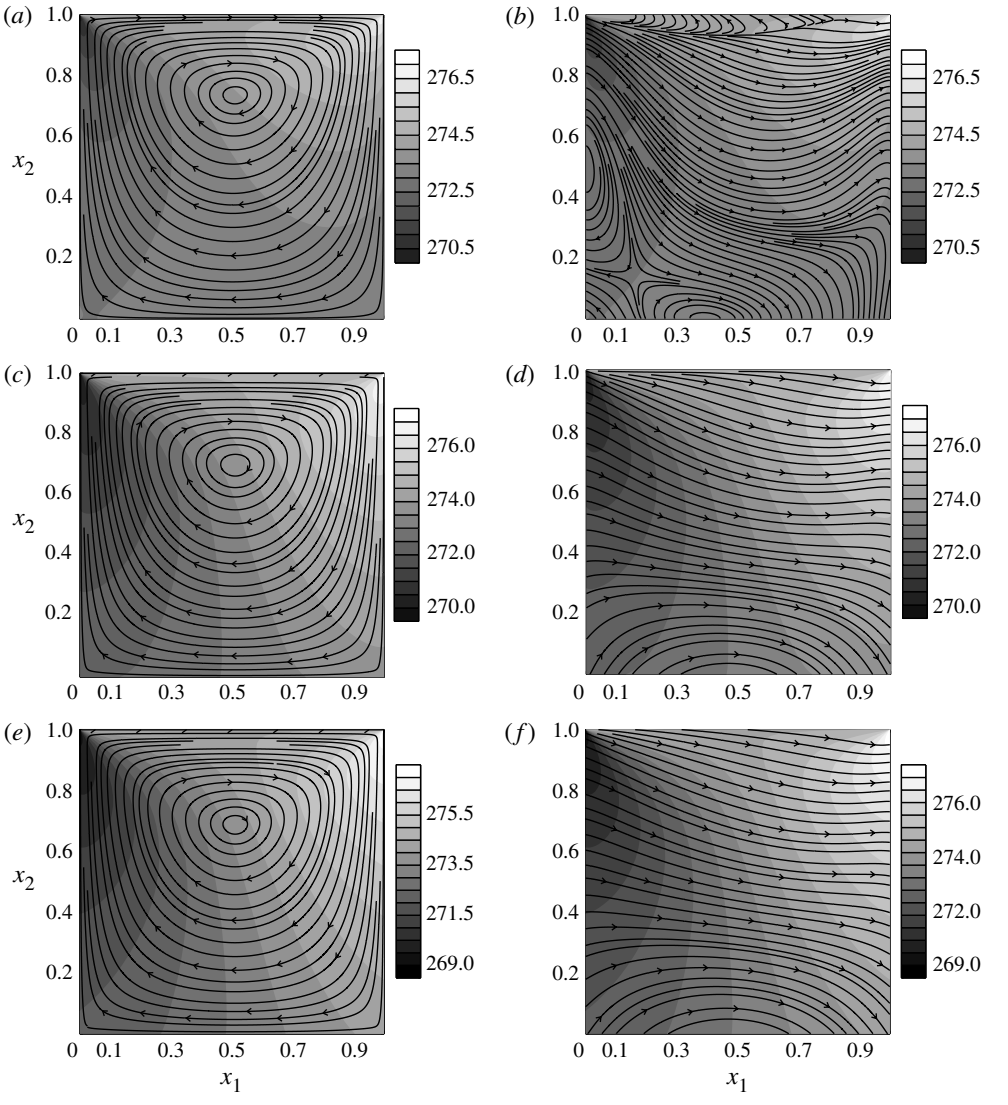


FIGURE 6. Temperature contours and streamlines (velocity: left-hand column; heat flux: right-hand column) in the lid-driven cavity flow of argon gas. The Knudsen number Kn_{vhs} is: (*a,b*) 0.1, (*c,d*) 1, and (*e,f*) 10. The lid moves from left to right, and the temperature is not normalised.

5.2. *Thermally driven flows*

5.2.1. *Thermal creep flow inside a closed channel*

Consider thermal creep flow in a two-dimensional closed rectangular channel with a length-to-width ratio of 5. The temperature at the right-hand side is set to be twice that of the left-hand side, while the temperature of the top and bottom walls varies linearly along the channel. Using the mean density, the temperature of the left-hand wall, and the channel width, *Kn* is set to be 0.08, 0.2, 0.25, 0.6, 2, and 10 in the cases we investigate. Figure 8 presents the resulting streamlines and the temperature distributions inside the channel for the flow of argon gas. Due to symmetry, only the

https://doi.org/10.1017/jfm.2014.79 Published online by Cambridge University Press

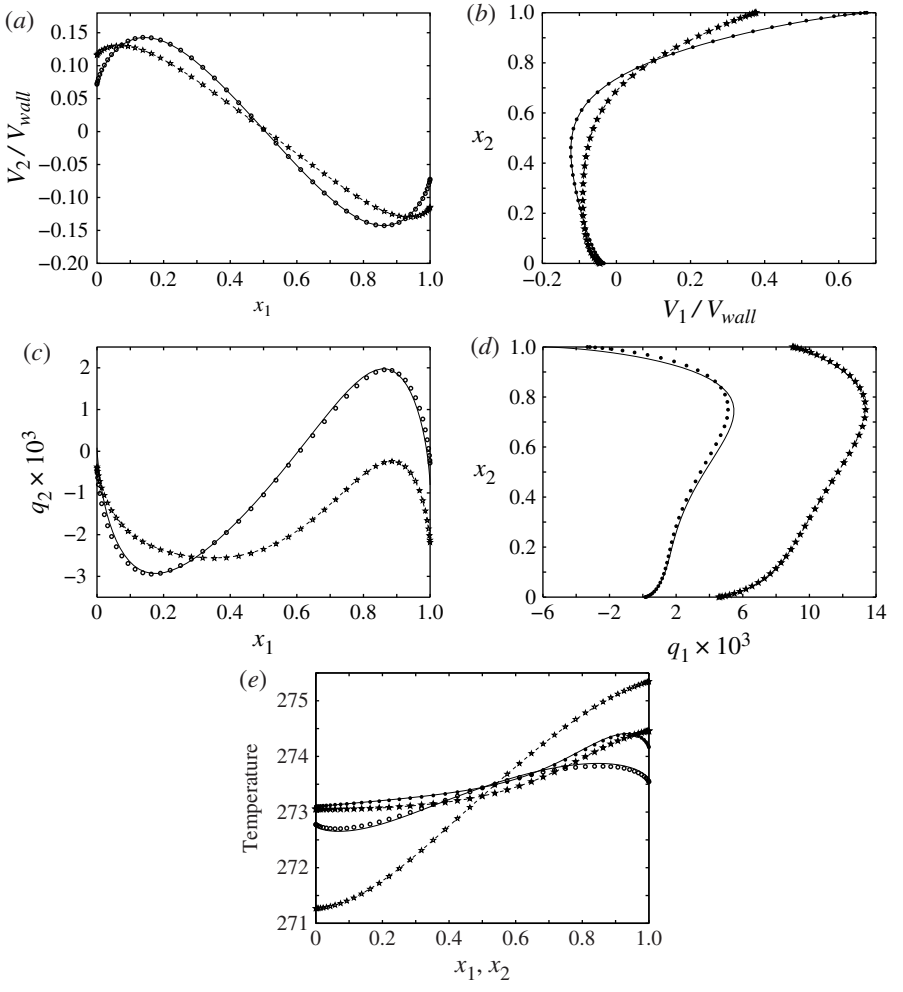


FIGURE 7. Comparisons of the velocity, heat flux, and temperature profiles between argon and hard-sphere gases in lid-driven cavity flow. The solid (or dashed) lines are the results for argon with $Kn_{vhs} = 0.1$ (or 10). The circles (or stars) are the results for the hard-sphere gas with $Kn_{vhs} = 0.132$ (or 13.2). (*a,c*) at $x_2 = 0.5$. (*b,d*) at $x_1 = 0.5$. (*e*) Filled (open) markers: $x_1 = 0.5$ ($x_2 = 0.5$).

lower half of the spatial domain is shown. Unlike thermal creep in an open channel, where the flow straightforwardly moves towards the hot region, the thermal creep flow in a closed channel exhibits richer phenomena. At $Kn = 0.08$, the gas flows from the cold region to the hot region along the bottom wall, and returns in the central region. At $Kn = 0.2$, the flow still moves from hot to cold in the central region; however, near the lower wall the flow moves towards the hot region when $x_1 < 2$ and towards the cold region for $x_1 > 2$, i.e. a circulation emerges near the lower hot corner of the domain. At $Kn = 0.25$, the circulation near the lower wall grows, which divides the flow in the central region into two circulation zones. The lower circulation zone keeps expanding, and pushes the other two circulations in the central region towards the left- and right-hand boundaries, as Kn increases. At $Kn = 0.6$, the flow direction is reversed (as compared to that when $Kn = 0.08$) and only one circulation zone remains near the left-hand wall. The reversal of the flow direction

https://doi.org/10.1017/jfm.2014.79 Published online by Cambridge University Press

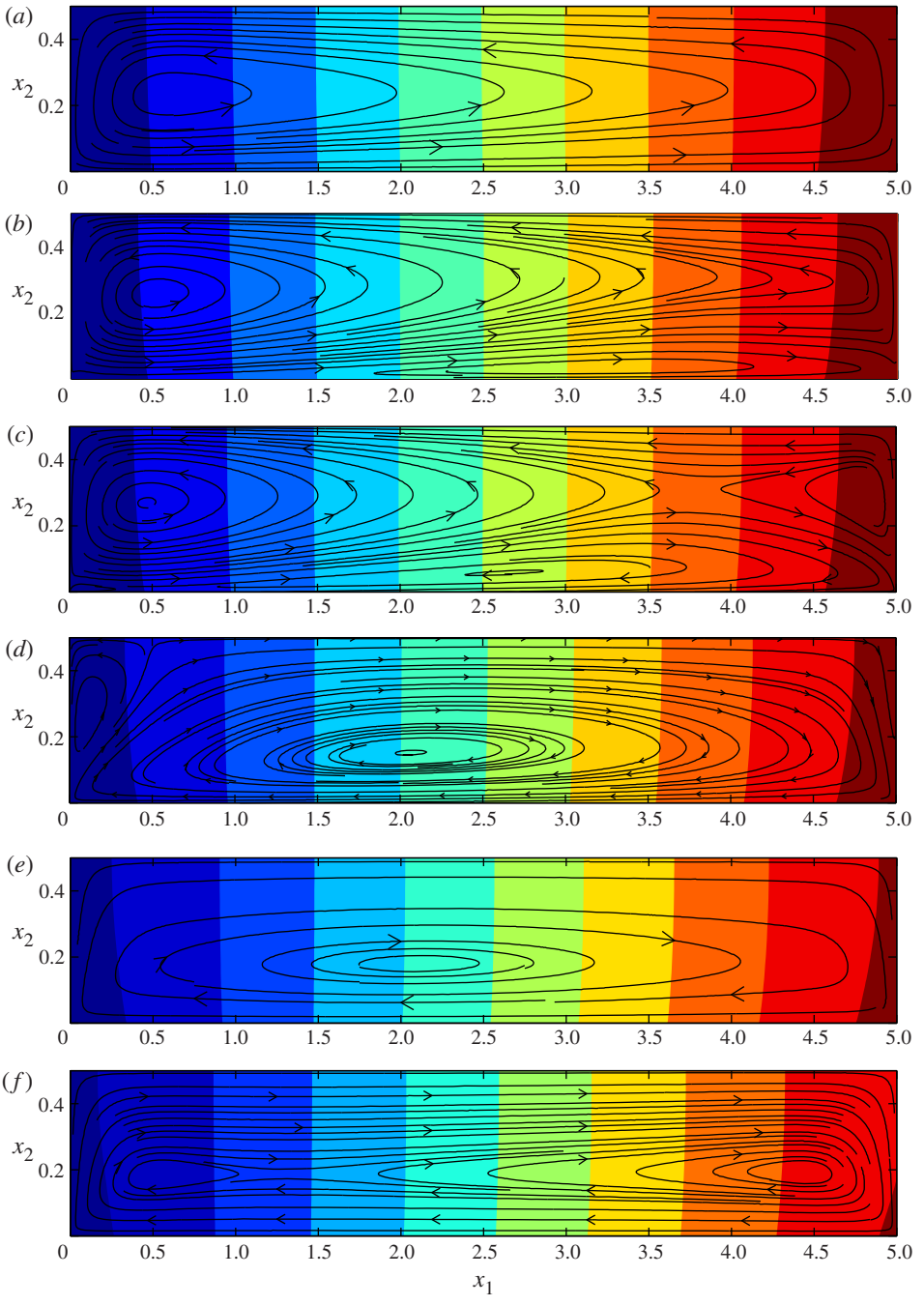


FIGURE 8. (Colour online) Temperature contours and velocity streamlines in the thermal creep flow of argon gas within a closed rectangular channel (only the lower half-domain is shown). In each figure, from left to right, the non-dimensional temperature of each contour is $1+0.1i$, where $i=1,2,\ldots,9$. (*a*) $Kn=0.08$, (*b*) $Kn=0.2$, (*c*) $Kn=0.25$, (*d*) $Kn=0.6$, (*e*) $Kn=2$, (*f*) $Kn=10$.

https://doi.org/10.1017/jfm.2014.79 Published online by Cambridge University Press

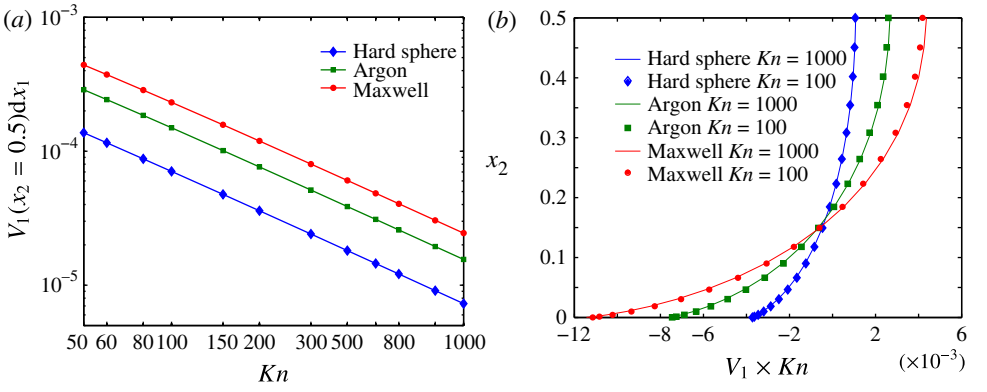


FIGURE 9. (Colour online) (*a*) The horizontal velocity varying with Kn in thermal creep flow inside a closed rectangular channel, in the free-molecular regime. In this double-logarithmic diagram, the three lines have a slope of 1, demonstrating that the velocity magnitude is proportional to $1/Kn$. (*b*) Examples of the linear scalability in the free-molecular regime of the horizontal velocity at $x_1 = 1.4825$.

persists but the circulations near the left-hand wall gradually disappear as the Knudsen number increases further, for instance, to $Kn = 2$. By $Kn = 10$, the gas near the bottom wall moves from hot to cold, and two clockwise circulations emerge near the left- and right-hand sides. Finally, when the flow enters the free-molecular regime, the streamline pattern does not change, but the velocity magnitudes are proportional to $1/Kn$, see figure 9. The magnitudes of density, pressure, and temperature, however, remain unchanged irrespective of the Knudsen number in this regime.

Comparison of the velocity profiles for different molecular models at the start and the end of the transition flow regime are shown in figure 10; it can be seen that the molecular model affects the velocity magnitudes significantly.

The flow patterns shown in figure 8 can be understood qualitatively as follows. Starting from the global equilibrium state, the temperature gradient drives the gas molecules to move from cold to hot (thermal creep flow). This process increases the pressure at the right-hand side of the channel while decreasing the pressure at the left. Then, the pressure gradient causes the gas molecules to move to the left (Poiseuille flow). The steady state is reached when the effects of Poiseuille and thermal creep flows cancel each other out, that is, when the net mass flow rate across the lines perpendicular to the top and bottom walls is zero. The horizontal velocity profile can be analysed by assuming the wall temperature gradient to be small (i.e. the channel is long enough) so that the BE can be linearized. In this case, we can directly use the velocity profiles obtained in § 4. Figure 11 plots the net velocity profiles in the linear superposition of Poiseuille and thermal creep flows between parallel plates where the net mass flow rate is zero. The flow velocities are normalized; in real problems, the horizontal velocity is given by (see the first paragraph in § 4.2):

$$V_1 = \beta_T \left\{ V_1[h_T] - \frac{\mathscr{M}[h_T]}{\mathscr{M}[h_P]} V_1[h_P] \right\}, \tag{5.2}$$

where β_T is the temperature gradient; in this case, it is about $1/5$.

Now the horizontal velocity profiles in figure 11 can be used to explain the flow patterns in figure 8. From figure 11 we find that, when $Kn = \sqrt{\pi}/20$, the

https://doi.org/10.1017/jfm.2014.79 Published online by Cambridge University Press

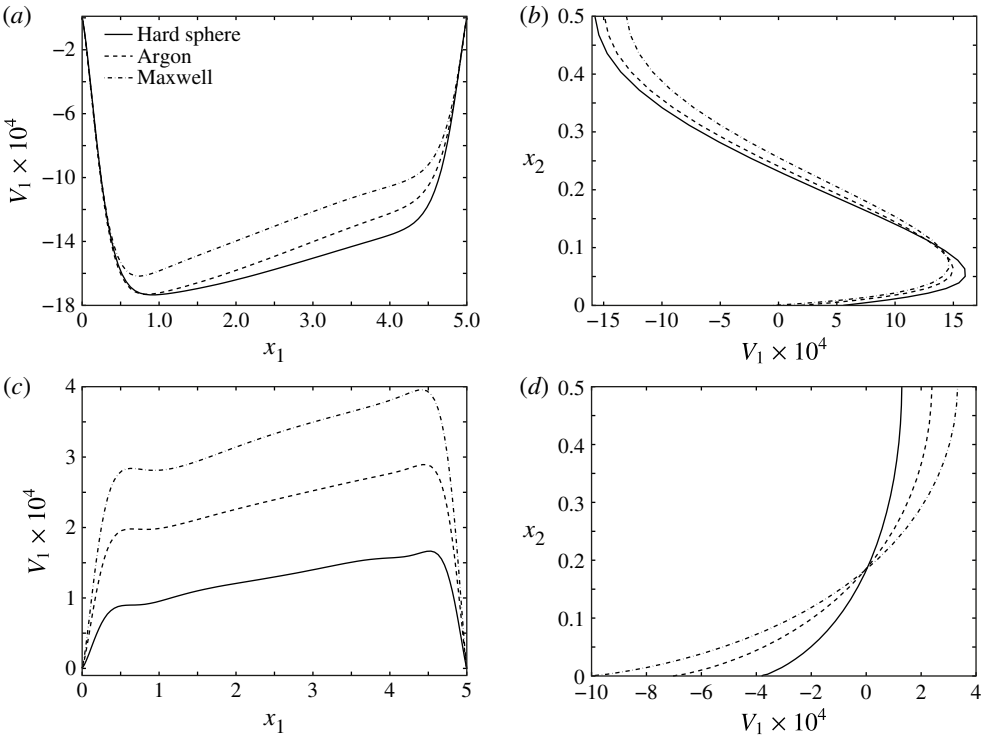


FIGURE 10. Velocity profiles for thermal creep flow within a closed rectangular channel; (*a,b*) $Kn = 0.08$, and (*c,d*) $Kn = 10$ are represented by the red and blue lines and axis labels, respectively. (*a,c*) Horizontal velocity along the central horizontal line. (*b,d*) Horizontal velocity along the central vertical line.

net horizontal velocity is positive when $x_2 < 0.25$ and negative otherwise, which agrees well with the flow pattern in figure 8(*a*). Also, from figure 10(*a*) we find that, at $Kn = 0.08$, $V_1(x_2 = 0.5) \simeq -0.0018$ near the left-hand side of the channel, which is well predicted by (5.2) when we choose $Kn = \sqrt{\pi}/20$ and $x_2 = 0.5$: $V_1(x_2 = 0.5) \simeq (-0.009)/5 = -0.0018$. Furthermore, as Kn increases, the magnitude of the horizontal velocity at $x_2 = 0.5$ decreases (figure 11). This is in accordance with the horizontal velocity profiles shown in figure 10(*a*), where the velocity magnitude decreases as x_1 increases from 1 to 4, because the local Knudsen number increases along the channel as a result of increasing temperature and decreasing particle number density. When $Kn = \sqrt{\pi}/10$ (and $\sqrt{\pi}/8$), the net horizontal velocity in figure 11 is positive when $0.26 > x_2 > 0.009$ (and $0.28 > x_2 > 0.023$) and negative otherwise. This explains the flow patterns at the right-hand side of the channel, as shown in figure 8(*b*). As Kn increases, the extent of the region near the bottom wall where the velocity is negative increases (figure 11), so that the circulation near the bottom wall in figure 8(*c*) is larger than that in figure 8(*b*). When Kn increases above a critical value of around $\sqrt{\pi}/5$, the horizontal velocity in figure 11 is negative when x_2 is smaller than some fixed value x_{2c} and positive otherwise. In this case, the flow direction is completely reversed in comparison with that at small Knudsen numbers. When $Kn > \sqrt{\pi}/2$, the fixed value is $x_{2c} = 0.2$. In figure 8(*d–f*), we see that the gas moves from left to right if $x_2 < 0.2$, and moves right to left if $x_2 > 0.2$.

https://doi.org/10.1017/jfm.2014.79 Published online by Cambridge University Press

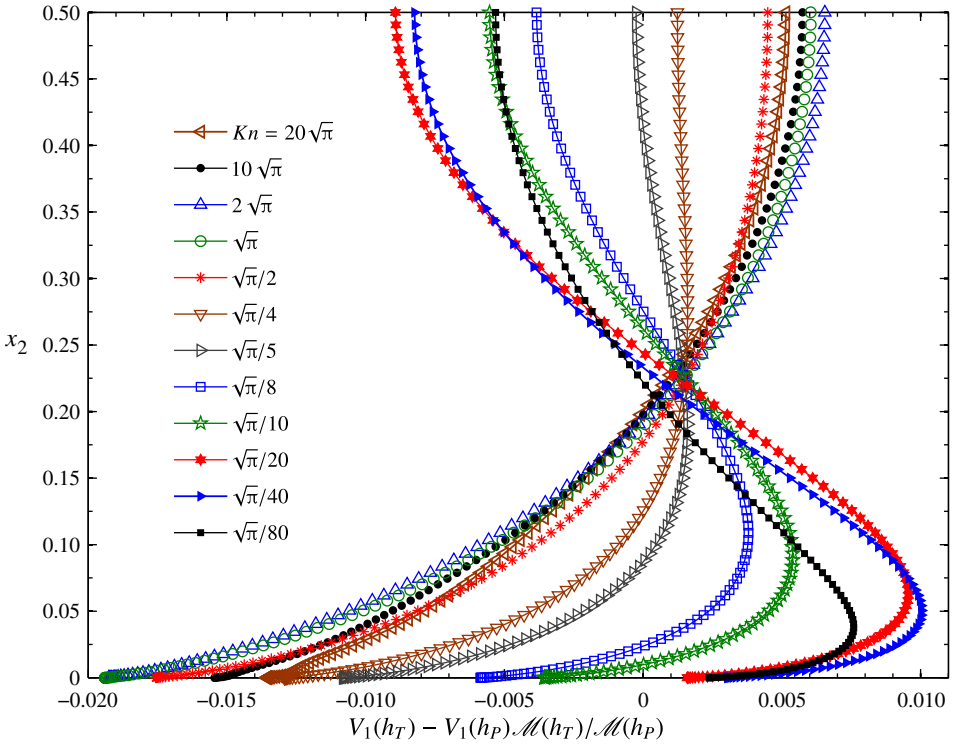


FIGURE 11. (Colour online) Net horizontal velocity profiles obtained by linear superposition of the velocity profiles of Poiseuille and thermal creep flows between parallel plates, which result in zero mass flow rate. The walls are at $x_2 = 0$ and $x_2 = 1$ and the working gas is argon, where the IPL model with $\omega = 0.81$ is used.

Note that the above analysis is valid at positions far from the left- and right-hand walls; near the ends of the channel, the horizontal velocity is nearly zero and the above analysis fails. This end effect becomes dominant in the whole channel when the molecular mean free path is of the order of half the distance between the left- and right-hand walls. When the mean free path is much larger than the wall distance, from figures 8 and 9 we find that the streamline pattern does not change very much, but the velocity magnitude is inversely proportional to the Knudsen number. In other words, at large Knudsen numbers, the flow pattern is determined by the velocity profiles in figure 11 at a critical Knudsen number. In our numerical simulations, we find that the critical Knudsen number varies linearly with the length-to-height ratio A of the channel:

$$Kn_c \simeq 0.35A. \tag{5.3}$$

For instance, when $A = 0.25$, the end effect becomes dominant when $Kn_c \geqslant 0.09$, and the flow pattern at $Kn \gg Kn_c$ is similar to the flow pattern at Kn_c. Figure 11 shows that at $Kn = 0.09$ the molecules move from left to right near the bottom wall, and return to the left at $x_2 = 0.5$, which is exactly the case shown in figure 12(*a*). For $A = 0.5$, $Kn_c = 0.18 \simeq \sqrt{\pi}/10$, and from figure 11 we see the horizontal flow velocity turns from negative to positive and then back to negative as we move from the bottom wall to the central region, which is the same as in figure 12(*b*). The aspect ratio $A = 1$ is a critical case, since near $Kn_c = 0.35 \simeq \sqrt{\pi}/5$, the horizontal velocity at $x_2 = 0.5$ could

https://doi.org/10.1017/jfm.2014.79 Published online by Cambridge University Press

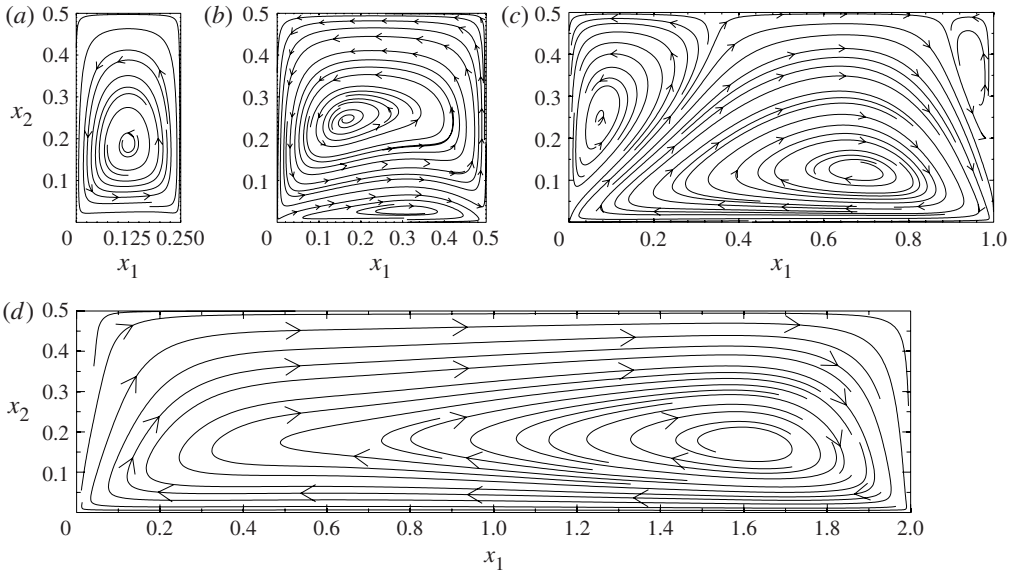


FIGURE 12. Thermal creep flow patterns of argon gas (IPL model with $\omega = 0.81$) in the free-molecular regime at different values of length-to-height ratio A: (a) $A = 0.25$, (b) $A = 0.5$, (c) $A = 1$, and (d) $A = 2$.

be negative or positive, depending on whether the local Knudsen number is smaller or larger than $\sqrt{\pi}/5$. That is why the flow pattern shown in figure 12(c) is more complicated. For $A = 2$, where $Kn_c = 0.7$, the flow pattern is simpler, and the molecules move from the hot to the cold region near the bottom and return from the cold to the hot region near $x_2 = 0.5$, see figure 12(d). For $Kn < Kn_c$, the horizontal velocity profiles can be analysed using the data in figure 11.

5.2.2. *Flow induced by a spatially periodic wall temperature*

Consider the gas flow between two parallel plates that have a spatially periodic temperature: the upper ($x_2 = \ell$) and lower plates ($x_2 = 0$) have the temperature $T_0(1 - 0.5\cos 2\pi x_1)$. Due to symmetry, the spatial domain is chosen as $0 \leqslant x_1, x_2 \leqslant 1/2$. The specular reflection boundary condition is chosen for the left-hand, upper, and right-hand boundaries, while the diffuse boundary condition is employed at the lower wall. Using the mean density, mean temperature T_0, and the wall distance ℓ, the unconfined Knudsen number Kn is chosen to be 0.1, 1, and 10. In the spatial discretization, 51 equispaced points are used in the x_1 direction and 51 non-uniform points (see (4.2)) are placed in the x_2 direction, with most of the points close to the lower wall. In the discretization of the velocity space, $64 \times 64 \times 16$ (maximum velocity $L = 7.5$, $L_2 = 5$ in (4.3) with $\iota = 3$) grid points are used when $Kn = 0.1$ and 1, while $128 \times 128 \times 16$ grid points are used when $Kn = 10$. The number of frequency components is $32 \times 32 \times 32$. Even with such a large number of velocity grid points, the FSM with $M = 6$ takes only $\sim$150 min to converge to $\|\epsilon\|_2$ less than 10^{-5} at $Kn = 0.1$.

The temperature contours and velocity streamlines are shown in figure 13. The gas moves from the cold to the hot region near the lower wall, while it returns from hot to cold around the central horizontal region. The circulation centre approaches the lower wall as Kn increases. The marginal VDFs, which become more complicated as Kn increases, are shown in figure 14, and large discontinuities at the lower wall

https://doi.org/10.1017/jfm.2014.79 Published online by Cambridge University Press

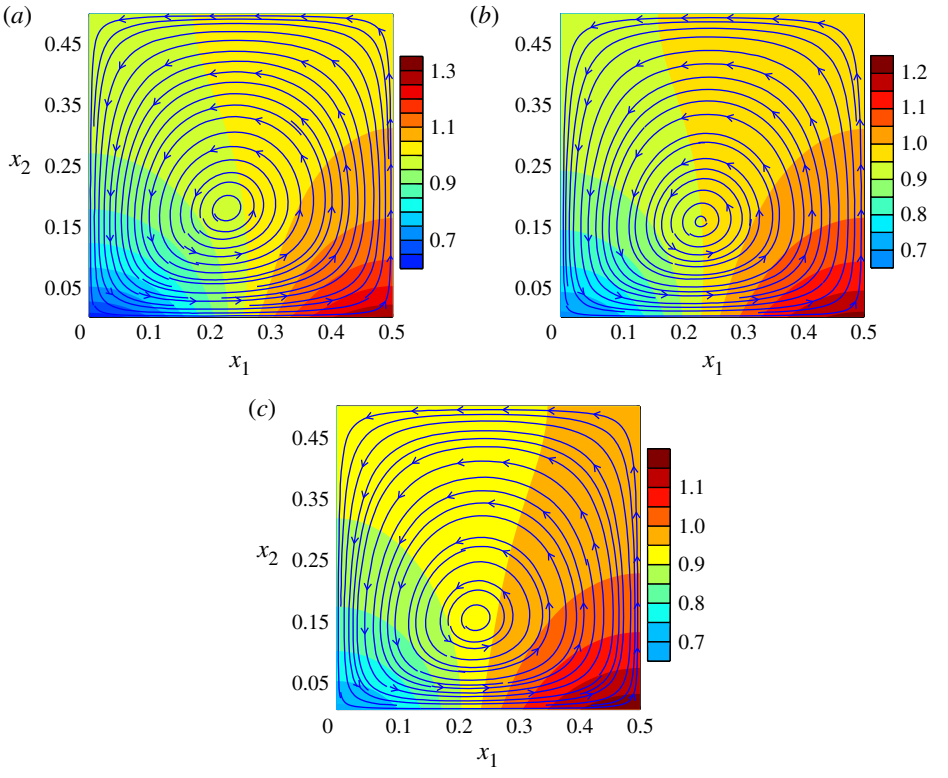


FIGURE 13. Contour plots of the temperature, and the velocity streamlines in argon gas subjected to a spatially periodic wall temperature: (*a*) $Kn = 0.1$, (*b*) $Kn = 1$, (*c*) $Kn = 10$.

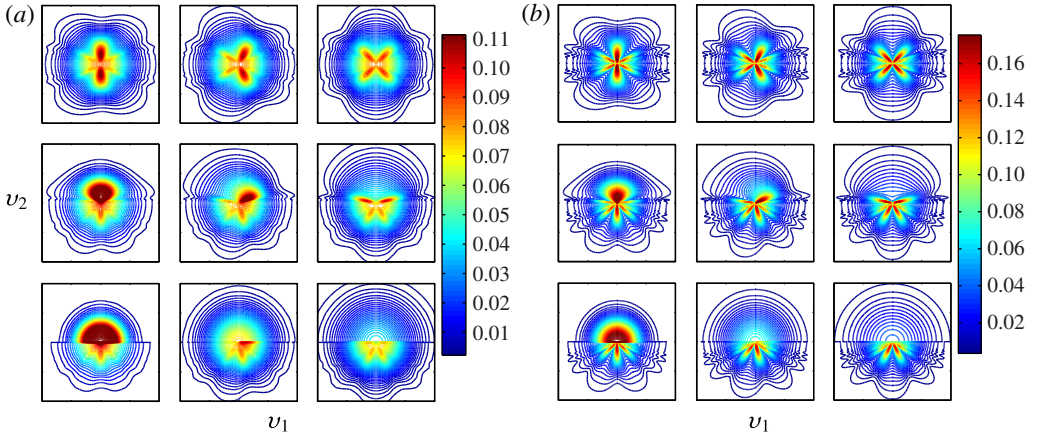


FIGURE 14. Contour plots of the marginal VDF, $\int f \mathrm{d}v_3$, for hard sphere gas for (*a*) $Kn = 1$ and (*b*) $Kn = 10$. In each figure, from bottom to top, $x_2 = 0.5$, 0.25, and 0.5, respectively; from left to right, $x_1 = 0$, 0.25, and 0.5, respectively. The velocity region shown is $[-2, 2] \times [-2, 2]$.

and fine structures are clearly seen. This demonstrates the necessity of using a large number of velocity grid points in the v_1 and v_2 directions at large Kn, in order to get

https://doi.org/10.1017/jfm.2014.79 Published online by Cambridge University Press

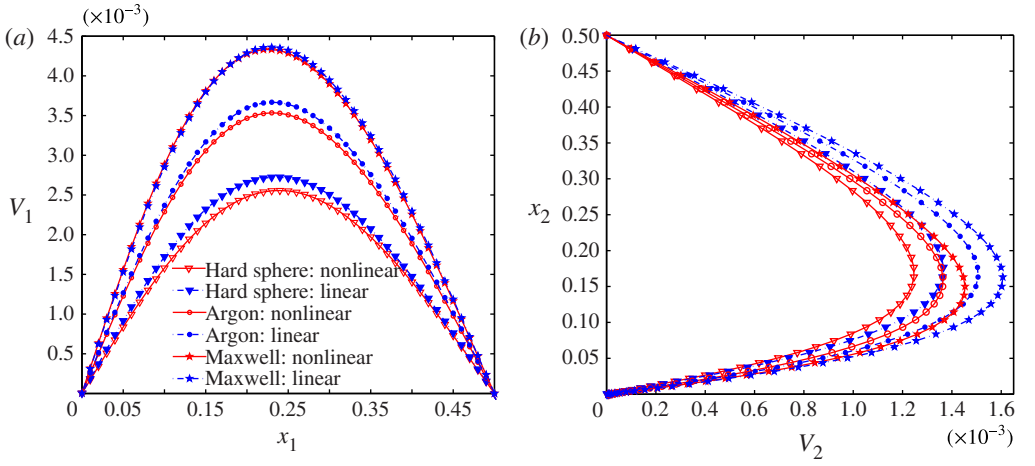


FIGURE 15. (Colour online) Comparisons of the velocity profiles predicted by the full nonlinear and the linearized BEs, and for different molecular models. The unconfined Knudsen number is $Kn = 1$ and the temperature of the top and bottom walls varies as $T_0(1 - 0.5\cos 2\pi x_1)$. (*a*) $x_2 = 0$, (*b*) $x_1 = 0.5$.

a high resolution. The flow velocities for different molecular models are compared in figure 15: the maximum velocity increases with the viscosity index. We have also investigated the flow in the free-molecular regime and find that the velocity magnitudes are inversely proportional to the Knudsen number, as was the case for thermal creep flow inside closed channels.

Note that this problem has also been solved by the low-noise DSMC method, based on the linearized BE (Radtke *et al.* 2011): from figure 14 we see that the VDFs deviate significantly from the equilibrium state, so the required linearization around the global equilibrium state may not be appropriate. We test this by solving the linearized BE using the same spatial and velocity grids. Although the velocity is very small, the numerical comparisons shown in figure 15 indicate that linearization around the global state does not give accurate results in this problem if the variation of the wall temperature is strong. If the temperature variation is weak, e.g. the wall temperature is $T_0(1 - 0.05\cos 2\pi x_1)$, however, the linearized BE can be used effectively.

5.2.3. *Flow induced by a temperature discontinuity*

Finally, we consider the gas flow inside a square box that is driven by a temperature discontinuity: the temperature of the left-hand wall is one half that of the other three walls. In terms of the mean density, temperature of the left-hand wall, and the wall distance, Kn is 0.1, 1, and 10 in the cases we investigate. Half the spatial region ($0 \leqslant x_1 \leqslant 1$, $0 \leqslant x_2 \leqslant 0.5$) is simulated, due to symmetry. The non-uniform spatial grids are 101×100 for $Kn = 0.1$, and 51×30 for $Kn = 1$ and 10. The velocity grids are $48 \times 48 \times 12$ for $Kn = 0.1$ and 1, and $64 \times 64 \times 12$ for $Kn = 10$. The resulting temperature contours and velocity streamlines for a Maxwell gas in this configuration are shown in figure 16. At $Kn = 0.1$, four circulation zones arise. As Kn increases, the two circulations near the left- and the right-hand walls gradually disappear, while the centre of the largest circulation moves towards the right-hand wall. Note that this problem was previously studied using the original DSMC method (Huang, Xu & Yu 2013), and comparison shows that our FSM yields much smoother streamlines than the DSMC method at $Kn = 0.1$.

https://doi.org/10.1017/jfm.2014.79 Published online by Cambridge University Press

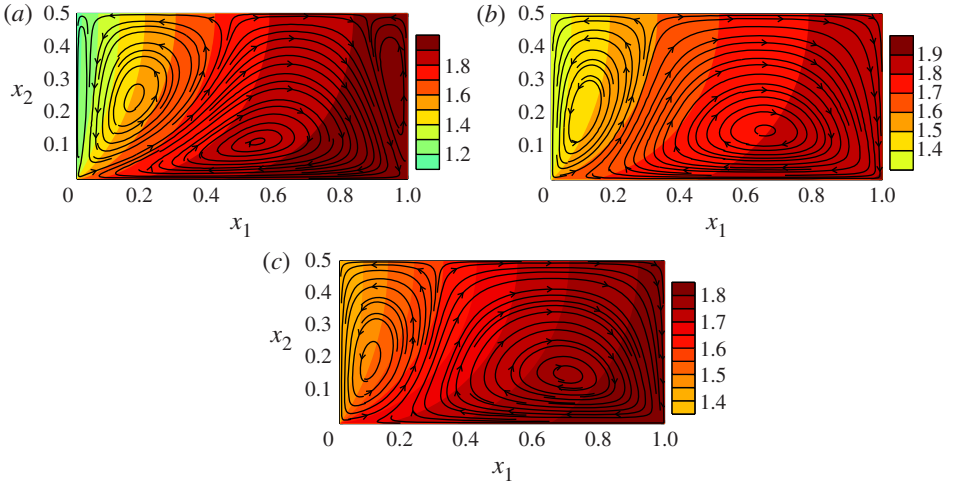


FIGURE 16. (Colour online) Temperature contours and velocity streamlines in the flow in a square box of a Maxwell gas driven by a temperature discontinuity at the bottom left corner: (*a*) $Kn = 0.1$, (*b*) $Kn = 1$, (*c*) $Kn = 10$.

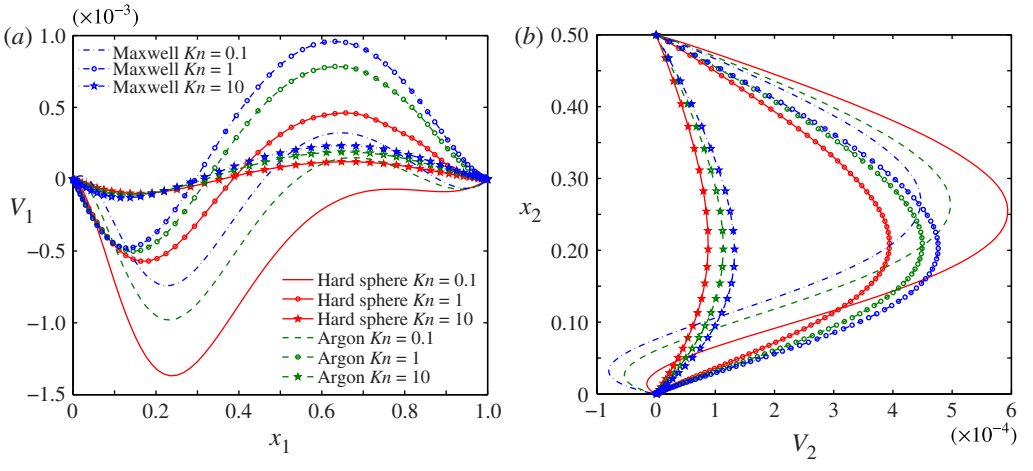


FIGURE 17. (Colour online) Comparison of the velocity profiles for different molecular models for the flow in a square box driven by a temperature discontinuity at the corner. (*a*) Velocity along the central horizontal line. (*b*) Velocity along the central vertical line.

The velocity profiles along the central horizontal and vertical lines are depicted in figure 17, and clearly show the influence of different molecular models. However, interestingly, the molecular model has little effect on the temperature and heat flux profiles (not shown). We have also solved this problem using the BGK model, and found that while the BGK model gives almost identical temperature and heat flux profiles, it cannot recover the velocity profiles.

In the free-molecular limit, the density, pressure, and temperature profiles reach fixed values independent of the Knudsen number. The streamline pattern also remains unchanged, except that the velocity magnitudes decrease as $1/Kn$.

https://doi.org/10.1017/jfm.2014.79 Published online by Cambridge University Press

6. Conclusions

We have studied the application and usefulness of the FSM for gas microflow simulations. A numerical approximation to both the linearized and nonlinear Boltzmann collision operator was presented. Numerical accuracy has been evaluated by comparing our FSM results with the numerical kernel method for Poiseuille flow, and excellent agreements in the mass and heat flow rates were seen up to $Kn \sim 10^6$. Computational efficiency has been demonstrated on two-dimensional Poiseuille and lid-driven cavity flows, and we found that the FSM can be 10–50 times faster than the low-noise DSMC method (which itself is much faster than the original DSMC technique for microflow simulations).

We have investigated the influence of different molecular models on the mass and heat flow rates in Poiseuille and thermal creep flows between parallel plates. The mechanism of the variability in flow rates for different molecular models with the same value of shear viscosity is explained in terms of the effective collision frequency. We also assessed the accuracy of special collision kernels for the LJ potential, and found that these can produce mass and heat flow rates with a relative error of less than 2 % for $Kn < 22$ and $\sim$5 % at $Kn \simeq 88$, when compared to results obtained using the realistic LJ potential; for the flow along a rectangular channel, this relative error decreases as the aspect ratio decreases from infinity to 1.

We have simulated a number of two-dimensional microflows. New insight into experimental mass flow rates along a rectangular tube with a large aspect ratio (Ewart *et al.* 2007) has been provided. We have also analysed quantitatively the influence of different molecular models on the flow properties. In lid-driven cavity flow, we found that the solution is only determined by the value of the shear viscosity, irrespective of the molecular model. For thermally driven flows, however, the molecular model affects the flow velocity significantly, but the temperature field is not very sensitive to the molecular model. In the free-molecular regime, our numerical results showed that the streamline pattern does not change but the velocity magnitudes are inversely proportional to the Knudsen number. We have also analysed in detail the thermal creep flow inside a closed rectangular channel, and found that the streamline pattern can be predicted based on the velocity profiles of superposed Poiseuille and thermal creep flows between parallel plates. These thermally driven flows can serve as benchmark cases for future investigations.

Finally, we brief analyse why the FSM is suitable for the simulation of moderately and/or highly rarefied microflows. The molecular velocity distribution functions have large discontinuities at large Kn, hence a significant number of velocity grids are needed. This poses an extremely difficult problem for other deterministic methods that handle binary collisions in velocity space. However, this problem is amenable for the FSM because the collisions are treated in frequency space. The FSM approximates the collision operator with spectral accuracy (Mouhot & Pareschi 2006); the number of frequency components does not need to be as large as the velocity grids. One reason for this is that discontinuities in the distribution function produce high-frequency components in its spectrum (and this is usually smooth, or at least smoother than the distribution function); in the calculation of the spectrum of the collision operator, the spectrum of the distribution function is multiplied by a weight function which is very small for high-frequency components (see figure 4 in Wu *et al.* 2013). Therefore, very high frequencies can be safely ignored: in the transition flow regime, we have shown that 32 frequency components in each direction is enough.

The only drawback of the FSM, like all other deterministic numerical methods, is that a large amount of computer memory is required (relative to that required for the DSMC method).

https://doi.org/10.1017/jfm.2014.79 Published online by Cambridge University Press

Acknowledgements

Y.Z. thanks the UK's Royal Academy of Engineering (RAE) and the Leverhulme Trust for the award of a RAE/Leverhulme Senior Research Fellowship. This work is financially supported by the UK's Engineering and Physical Sciences Research Council (EPSRC) under grants EP/I036117/1 and EP/I011927/1. The authors also thank the reviewers of this paper for their helpful comments.

REFERENCES

BAKER, L. L. & HADJICONSTANTINOU, N. G. 2005 Variance reduction for Monte Carlo solutions of the Boltzmann equation. *Phys. Fluids* **17** (5), 051703.

BIRD, G. A. 1994 *Molecular Gas Dynamics and the Direct Simulation of Gas Flows*. Oxford University Press.

CERCIGNANI, C. 1990 *Mathematical Methods in Kinetic Theory*. Plenum.

CERCIGNANI, C. & DANERI, A. 1963 Flow of a rarefied gas between two parallel plates. *J. Appl. Phys.* **34**, 3509–3513.

CHAPMAN, S. & COWLING, T. G. 1970 *The Mathematical Theory of Non-uniform Gases*. Cambridge University Press.

DOI, T. 2010 Numerical analysis of the Poiseuille flow and thermal transpiration of a rarefied gas through a pipe with a rectangular cross-section based on the linearized Boltzmann equation for a hard-sphere molecular gas. *J. Vac. Sci. Technol.* A **28**, 603–612.

DOI, T. 2012*a* Effect of weak gravitation on the plane Poiseuille flow of a highly rarefied gas. *Z. Angew. Math. Phys.* **63**, 1091–1102.

DOI, T. 2012*b* Plane thermal transpiration of a rarefied gas in the presence of gravitation. *Vacuum* **86**, 1541–1546.

EWART, T., PERRIER, P., GRAUR, I. A. & MÉOLANS, J. G. 2007 Mass flow rate measurements in a microchannel, from hydrodynamic to near free molecular regimes. *J. Fluid Mech.* **584**, 337–356.

FAN, J. & SHEN, C. 2001 Statistical simulation of low-speed rarefied gas flows. *J. Comput. Phys.* **167**, 393–412.

FRANGI, A., GHISI, A. & FREZZOTTI, A. 2007 Analysis of gas flow in MEMS by a deterministic 3D BGK kinetic model. *Sensor Lett.* **6** (1), 1–7.

FUNAGANE, H. & TAKATA, S. 2012 Hagen-Poiseuille and thermal transpiration flows of a highly rarefied gas through a circular pipe. *Fluid Dyn. Res.* **44**, 055506.

GAMBA, I. M. & THARKABHUSHANAM, S. H. 2009 Spectral-Lagrangian methods for collisional models of non-equilibrium statistical states. *J. Comput. Phys.* **228** (6), 2012–2036.

GARCIA-COLIN, L. S., VELASCO, R. M. & URIBE, F. J. 2008 Beyond the Navier–Stokes equations: Burnett hydrodynamics. *Phys. Rep.* **465**, 149–189.

GU, X. J. & EMERSON, D. R. 2009 A high-order moment approach for capturing non-equilibrium phenomena in the transition regime. *J. Fluid Mech.* **636**, 177–216.

HOMOLLE, T. M. M. & HADJICONSTANTINOU, N. G. 2007 A low-variance deviational simulation Monte Carlo for the Boltzmann equation. *J. Comput. Phys.* **226** (2), 2341–2358.

HUANG, J. C., XU, K. & YU, P. B. 2012 A unified gas-kinetic scheme for continuum and rarefied flows II: multi-dimensional cases. *Commun. Comput. Phys.* **12**, 662–690.

HUANG, J. C., XU, K. & YU, P. B. 2013 A unified gas-kinetic scheme for continuum and rarefied flows III: microflow simulations. *Commun. Comput. Phys.* **14**, 1147–1173.

JOHN, B., GU, X. J. & EMERSON, D. R. 2010 Investigation of heat and mass transfer in a lid-driven cavity under nonequilibrium flow conditions. *Numer. Heat Transfer* B **52**, 287–303.

JOHN, B., GU, X. J. & EMERSON, D. R. 2011 Effects of incomplete surface accommodation on non-equilibrium heat transfer in cavity flow: a parallel DSMC study. *Comput. Fluids* **45**, 197–201.

LOYALKA, S. K. 1971 Kinetic theory of thermal transpiration and mechanocaloric effect. I. *J. Chem. Phys.* **55**, 4497.

https://doi.org/10.1017/jfm.2014.79 Published online by Cambridge University Press

MASTERS, N. D. & YE, W. J. 2007 Octant flux splitting information preservation DSMC method for thermally driven flows. *J. Comput. Phys.* **226** (2), 2044–2062.

MIEUSSENS, L. & STRUCHTRUP, H. 2004 Numerical comparison of Bhatnagar–Gross–Krook models with proper Prandtl number. *Phys. Fluids* **16** (8), 2297–2813.

MOUHOT, C. & PARESCHI, L. 2006 Fast algorithms for computing the Boltzmann collision operator. *Maths Comput.* **75** (256), 1833–1852.

OHWADA, T., SONE, Y. & AOKI, K 1989 Numerical analysis of the Poiseuille and thermal transpiration flows between two parallel plates on the basis of the Boltzmann equation for hard-sphere molecules. *Phys. Fluids* A **1**, 2042–2049.

PARESCHI, L. & RUSSO, G. 2000 Numerical solution of the Boltzmann equation I: spectrally accurate approximation of the collision operator. *SIAM J. Numer. Anal.* **37** (4), 1217–1245.

RADTKE, G. A., HADJICONSTANTINOU, N. G. & WAGNER, W. 2011 Low-noise Monte Carlo simulation of the variable hard sphere gas. *Phys. Fluids* **23** (3), 030606.

RANA, A., TORRILHON, M. & STRUCHTRUP, H. 2013 A robust numerical method for the R13 equations of rarefied gas dynamics: application to lid driven cavity. *J. Comput. Phys.* **236**, 169–186.

SHARIPOV, F. 1994*a* Onsager-Casimir reciprocity relations for open gaseous systems at arbitrary rarefaction. I. General theory for single gas. *Physica* A **203**, 437–456.

SHARIPOV, F. 1994*b* Onsager–Casimir reciprocity relations for open gaseous systems at arbitrary rarefaction. II. Application of the theory for single gas. *Physica* A **203**, 457–485.

SHARIPOV, F. & BERTOLDO, G. 2009*a* Numerical solution of the linearized Boltzmann equation for an arbitrary intermolecular potential. *J. Comput. Phys.* **228**, 3345–3357.

SHARIPOV, F. & BERTOLDO, G. 2009*b* Poiseuille flow and thermal creep based on the Boltzmann equation with the Lennard-Jones potential over a wide range of the Knudsen number. *Phys. Fluids* **21**, 067101.

SHARIPOV, F. & SELEZNEV, V. 1994 Rarefied flow through a long tube at any pressure ratio. *J. Vac. Sci. Technol.* A **12** (5), 2933–2935.

SHARIPOV, F. & SELEZNEV, V. 1998 Data on internal rarefied gas flows. *J. Phys. Chem. Ref. Data* **27** (3), 657–706.

SHARIPOV, F. & STRAPASSON, J. L. 2012 *Ab initio* simulation of transport phenomena in rarefied gases. *Phys. Rev.* E **86**, 031130.

SHARIPOV, F. & STRAPASSON, J. L. 2013 Benchmark problems for mixtures of rarefied gases. I. Couette flow. *Phys. Fluids* **25**, 027101.

SONE, Y. 2002 *Kinetic Theory and Fluid Dynamics*. Birkhauser.

TAKATA, S. 2009*a* Note on the relation between thermophoresis and slow uniform flow problems for a rarefied gas. *Phys. Fluids* **21**, 112001.

TAKATA, S. 2009*b* Symmetry of the linearized Boltzmann equation and its application. *J. Stat. Phys.* **136**, 751.

TAKATA, S. & FUNAGANE, H. 2011 Poiseuille and thermal transpiration flows of a highly rarefied gas: over-concentration in the velocity distribution function. *J. Fluid Mech.* **669**, 242–259.

VENKATTRAMAN, A. & ALEXEENKO, A. A. 2012 Binary scattering model for Lennard-Jones potential: transport coefficients and collision integrals for non-equilibrium gas flow simulations. *Phys. Fluids* **24**, 027101.

WU, L., WHITE, C., SCANLON, T. J., REESE, J. M. & ZHANG, Y. H. 2013 Deterministic numerical solutions of the Boltzmann equation using the fast spectral method. *J. Comput. Phys.* **250**, 27–52.

https://doi.org/10.1017/jfm.2014.79 Published online by Cambridge University Press